

Rochester Institute of Technology

RIT Digital Institutional Repository

Theses

12-2016

A Study of Sintered Copper Porous Surfaces for Pool Boiling Enhancement

Felix Liu
ff13883@rit.edu

Follow this and additional works at: <https://repository.rit.edu/theses>

Recommended Citation

Liu, Felix, "A Study of Sintered Copper Porous Surfaces for Pool Boiling Enhancement" (2016). Thesis. Rochester Institute of Technology. Accessed from

This Thesis is brought to you for free and open access by the RIT Libraries. For more information, please contact repository@rit.edu.

A Study of Sintered Copper Porous Surfaces for Pool Boiling

Enhancement

by

Felix Liu

A Thesis Submitted in Partial Fulfillment of the Requirements for the Degree of

Master of Science in Mechanical Engineering

Approved by:

Dr. Satish Kandlikar

Primary Advisor – Dept. of Mechanical Engineering

Dr. Agamemnon Crassidis

Department Representative – Dept. of Mechanical Engineering

Dr. Michael Schrlau

Committee Member– Dept. of Mechanical Engineering

Dr. Michael Schertzer

Committee Member– Dept. of Mechanical Engineering

Thermal Analysis, Microfluidics, and Fuel Cell Laboratory

Department of Mechanical Engineering

Kate Gleason College of Engineering

Rochester, New York December 2016

Dedication

I would like to dedicate this work to God, and to my parents and to my family in Thermal Analysis, Microfluidics, and Fuel Cell Laboratory at RIT

Acknowledgements

Words cannot express the gratitude for the amount of support and encouragement that I have received while working as a graduate student in RIT. To everyone whom I worked with in the past few years, I want to say life will never be the same without you in my life. I would like to express my sincere gratitude to Dr. Satish Kandlikar for providing me the opportunity to pursue research in his renowned Thermal Analysis, Microfluidics, and Fuel Cell Laboratory and for mentoring me to cope with hardship in life. I would also like to thank Diane and Dr. Agamemnon Crassidis for providing the support from the department. Lastly I would like to thank my committee members Dr. Michael Schrlau and Dr. Michael Schertzer for providing guidance in ensuring the success of this work.

Abstract

Miniaturization in microelectronics demands effective thermal management from high energy density devices. While current cooling solutions employ single-phase heat transfer, they are often limited by high fluid temperature differences and pressure drops. Alternatively, two-phase cooling schemes offers attractive solutions to dissipate high heat fluxes at small temperature differences. Specifically, pool boiling has the potential to dissipate high heat fluxes without using pumps and other complex header configurations.

Two performance criterion that govern the heat transfer in pool boiling systems are the (i) Critical Heat Flux (CHF), and the (ii) Heat Transfer Coefficient. The CHF is the upper limit in nucleate boiling, while the Heat Transfer Coefficient dictates the efficiency of the process. The current thesis work relates to increasing the aforementioned parameters through copper porous coatings. In this work, copper substrates were coated with 3M copper powders using a drop coating and screen printing technique. Substrate bonding was achieved by sintering at elevated temperatures. The coated substrates were characterized using Scanning Electron Microscopy and Laser Confocal Microscopy which revealed the different geometrical parameters (pore sizes and coating thickness etc.) associated with the coatings. Pool boiling tests were conducted with distilled and degassed water at atmospheric pressure. A highest Critical Heat Flux (CHF) of 303 W/cm^2 was obtained on a test sample corresponding to a coating thickness of $447 \text{ }\mu\text{m}$. This translated to a CHF enhancement of $\sim 135 \%$ when compared to a plain copper surface. The effect of coating thickness on pool boiling performance was studied. High speed visualization was conducted on the test samples to identify underlying boiling mechanisms. The effect of additional nucleation sites, and wickability were evaluated in this study. The experimental observations were supplemented with analytical equations available in literature to identify driving mechanisms with the thin and thick porous coatings.

Table of Contents

Dedication	ii
Acknowledgements	iii
Abstract	iv
Table of Contents	iv
List of Figures	viii
List of Tables	xi
Nomenclature	xii
Chapter 1	1
1.1. Introduction	1
1.2. Boiling Curve	3
1.3. The Need for Enhancement	5
1.4. Micro-structured Surface Enhancement for Boiling	6
1.5. Porous Surfaces	7
Chapter 2 Literature Review	10
2.1. Sintering Process	10
2.2. Sintering as manufacturing techniques for porous surfaces	12
2.3. Coating Techniques	15

2.4.	Pool Boiling Performance Characteristics with Porous Surfaces and Water as Working Fluid.....	16
2.5.	Mechanism for boiling heat transfer enhancement.....	18
2.6.	Effect of Wickability on Pool Boiling Performance	20
2.7.	Scope of Work.....	22
Chapter 3	Experimental Work.....	23
3.1.	Sintering Process Set Up	23
3.2.	Test Set Up	24
3.3.	Test Samples.....	26
3.4.	Pool Boiling Procedure.....	27
3.5.	Data Analysis.....	28
3.6.	Uncertainty Analysis	30
3.7.	Drop Coating Technique	33
3.7.1	Sintering Process	34
3.7.2	Effect of Coating Thickness on Pool Boiling Performance using Drop Coating Technique	36
3.8.	Screen Printing Technique.....	39
3.8.1	Determination of Cu: Ink Mass Ratio	43
3.8.2	Effect of Coating Thickness on Pool Boiling Performance using Screen Printing Technique.....	45

3.8.3 Visualization Research	54
Chapter 4 Conclusion	69
4.1. Recommendations for Future Work	71

List of Figures

Fig. 1. Heat Transfer Coefficient Comparison for Various Cooling Methods [2]	1
Fig. 2.A Typical Pool Boiling Curve [3]	3
Fig. 3. Pictorial Representation of Boiling Enhancement	5
Fig. 4. Micro-Structured Surfaces [4]	7
Fig. 5. Schematic cross-section of a porous solid	8
Fig. 6. Scanning Electron Microscopic Images of the Sintering Neck Formation [9]	11
Fig. 7. Illustration of the sintering stages with a focus on the changes in porosity [9]	12
Fig. 8. Proposed Mechanism for Pool Boiling Enhancement with Porous Surfaces (Reproduced from [23])	19
Fig. 9. Sintering Set Up	24
Fig. 10. Pool Boiling Test Set Up	25
Fig. 11. Test Sample	26
Fig. 12. Schematics for data acquisition	28
Fig. 13. Uncertainty for Heat Flux	31
Fig. 14. Heat loss study showing temperature profile in the test sample	32
Fig. 15. Drop Coating Technique	34
Fig. 16. SEM Images At 1000X Showing Surfaces Sintered At Three Different Temperatures (Equipment: AMRAY 1830)	35

Fig. 17. SEM Image At 1000X Showing Large Pores Formed Using Lost Carbonate Sintering Process (Equipment: AMRAY 1830)	35
Fig. 18. Pool Boiling Curves using Distilled Water at Atm Pressure for Sintered Porous Surfaces Manufactured By Drop Coating And Lost Carbonate Process	36
Fig. 19. Variation of Heat Transfer Coefficient h with Heat Flux On Surfaces Using Drop Coating And Lost Carbonate Sintering Process	37
Fig. 20. Effect of Coating Thickness on CHF Drop Coating Technique	38
Fig. 21. Schematics of A Typical Screen Printing Process	39
Fig. 22. Summary of Manufacturing Process Using Screen Printing Technique	41
Fig. 23. Sintering Recipe for Screen Printing Technique	42
Fig. 24. XRD Results For A Sample Screen Printed Surface After Sintering	43
Fig. 25. LCM Images Showing Effect of Cu : Ink Mass Ratio on Morphology (a) SP_50. Cu : Ink 1:2 at 10X Magnification (b) SP_50 Cu : Ink 1:1 at 10X Magnification (c) SP_45 Cu: Ink 2:1 at 50X and 10X Magnification (Equipment : Keyence)	44
Fig. 26. LCM Images Showing the Thickness Uniformity of Sample Coating at 50X Magnifications (Equipment: Keyence) (a) SP_43 (b) SP_94 (c) SP_213	46
Fig. 27. SEM at 1000X Magnification Showing the Morphology of Sample test chips using 2:1 Cu: Ink Mass Ratio (a) SP_43 (b) SP_94 (c) SP_213 (Equipment AMRAY 1830)	47
Fig. 28. Pool Boiling Curves for Plain and Copper Porous Surfaces Created using Screen Printing Technique	48

Fig. 29. Heat Transfer Coefficient Comparison for Plain and Copper Porous Surfaces Created using Screen Printing Technique	49
Fig. 30. Effect of Coating Thickness on CHF Enhancement	50
Fig. 31. Measurement of Wickability using Sessile Drop Method	51
Fig. 32. Effect of Wickability and CHF Enhancement	52
Fig. 33. SP_28 Pool Boiling High Speed Images at Different Heat Fluxes 8000fps	54
Fig. 34. Dynamic Receding Contact Angle Measurement SP_28	56
Fig. 35. Range of Active Cavity Radii for a wall superheat SP_28	57
Fig. 36. SEM Image for SP_28 Showing Different Sizes of Cavity Radius	58
Fig. 37. CHF Visualization for Thin Coating (SP_ 28)	59
Fig. 38. High Speed Image showing Pool Boiling of SP_213 at Onset of Nucleation Boiling 8000 fps	61
Figure 39. High Speed Images Showing Pool Boiling of SP_213 at High Heat Fluxes 8000 fps	62
Figure 40. High Speed Images Showing SP_213 at CHF Condition 8000fps	64
Figure 41. Dynamic Receding Contact Angle Measurement for SP_213	65
Figure 42. Wickability Measurement Done by Rahman et al.[27]	66
Figure 43. Wicking Rate Calculated by Rate of Decrease in Contact Angle	66
Figure 44. Experimental CHF as a function of Wicked Volume Flux [27]	68

List of Tables

Table 1. Comparison of Sintering Process Used to Create Porous Surface	13
Table 2. Comparison of Coating Techniques	15
Table 3. Comparison of Pool Boiling Studies Using Water At Atm Pressure	17
Table 4. Wicking Characterization Methods of Micro Structured Surfaces	20
Table 5. Uncertainty Parameters	30
Table 6. Test Matrix for Drop Coating	33
Table 7. Cu: Ink Mass Ratio Study	44
Table 8. Test Matrix Effect of Coating Thickness	45
Table 9. Comparison of Wickability and CHF	52
Table 10. Parameters and Constants used for Water at Saturated Condition at Atmospheric Pressure Equation (7)	56
Table 11. Parameters and Constants involved with Kandlikar's Model [22]	60
Table 12. Parameters used to Calculated Predict CHF due to Capillary Wicking	67

Nomenclature

Saturation Pressure	P_{sat}
Saturation Temperature	T_{sat}
Latent Heat of Vaporization	h_{fg}
Density of Liquid	ρ_l
Density of Vapor	ρ_g
Surface Tension	σ
Dynamic Receding Contact Angle	θ_r
Acceleration due to gravity	g
Critical Heat Flux	CHF
Heat Transfer Coefficient	h
Heat Flux	q''

Chapter 1

This chapter provides the background and motivation for present work and a detailed description of the pool boiling curve and porous surfaces.

1.1. Introduction

The challenges in effective thermal management has gained tremendous attention in the field of high power microelectronic chips where heat dissipated from max power generation could cause the chips to exceed the max junction temperature allowed. This could result in issues in both product reliability and performance limitation. Additionally, increasing packing density, device speed, and integration of new materials with poor thermal properties contribute more heat generation to the chips while the max junction temperature allowed under industry guideline remains the same for more than 10 years. [1]

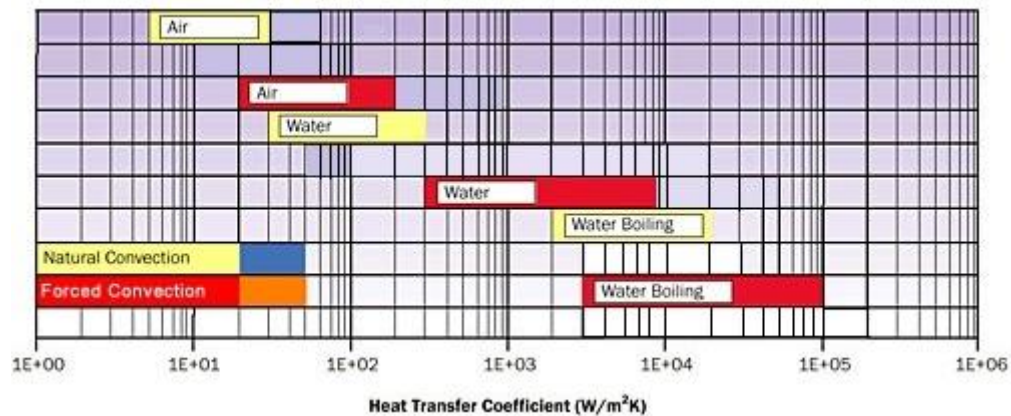


Fig. 1 Heat Transfer Coefficient Comparison for Various Cooling Methods [2]

Extensive research has been done in the field of heat transfer to address the need for effective thermal management in high end microelectronic devices. There are primarily

two schemes – single phase (air and liquid cooling) and two-phase (boiling). Fig. 1 shows comparison of Heat Transfer Coefficients (h) for both single and two phase cooling regimes. As we can see from the chart, two phase cooling (Boiling) stands out as an attractive method with h reaching the order of magnitude of $100,000 \text{ W/m}^2\text{K}$. Boiling is a phase-change process in which vapor bubbles are formed on a heated surface. Pool boiling refers to boiling on heated surface where the liquid flow is primarily governed by natural convection. In flow boiling, liquid is forced to flow over the heated surface using a pump. Currently, there are many companies that offer single and two phase liquid cooling as an option for high performance computers. Pool boiling is a simple technique without inclusion of complex header configurations and flow driving pumps. This is advantageous as it eliminates pumping power and significantly reduces operating costs. The challenge in such systems is to increase the heat flux dissipated to cater to a wide range of applications which is the main focus of this research study. This system takes the advantage of heat transfer enhancement through phase change (boiling) to effectively remove heat from the system. In addition, it provides valuable insights into understanding the fundamental mechanisms of boiling heat transfer.

1.2. Boiling Curve

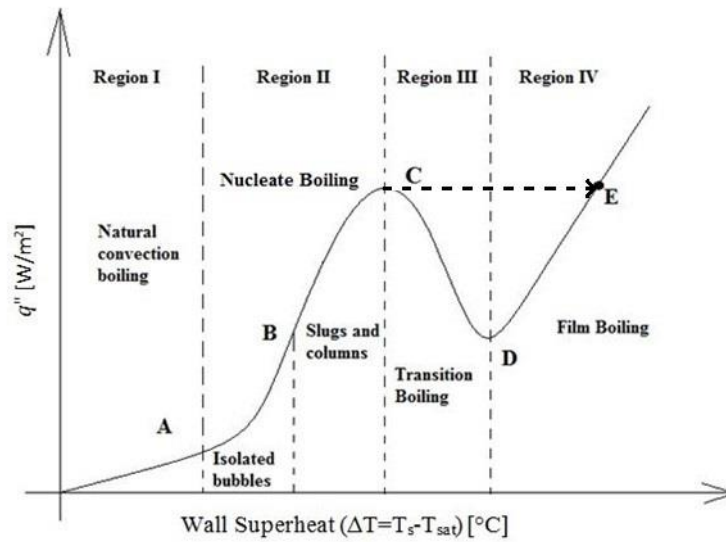


Fig. 2A Typical Pool Boiling Curve [3]

A pool boiling curve which relates the heat flux and wall superheat is typically used to characterize the boiling performance. Wall superheat is the difference between heater surface temperature and bulk liquid temperature in saturation. The pioneering study conducted by Nukiyama [3] resulted in the development of a pool boiling curve. In his study, a nichrome wire was heated and the boiling characteristics were captured for water. He identified four distinct boiling regimes, namely

1. Free Convection Boiling
2. Nucleate Boiling
3. Transition Boiling
4. Film Boiling

Fig. 2 is a typical pool boiling curve of saturated water that is obtained in a heat flux controlled system. To begin with, heat is supplied to a test sample, causing the surface temperature T_s to rise beyond the liquid saturation temperature to a temperature T_A . In this region, heat is removed through single-phase natural convection. Point A marks the onset of nucleate boiling at which boiling incipience starts at a nucleation site with the formation of a vapor bubble. The formation of this bubble is influenced by the capability of a cavity to entrap gas or vapor.

In the nucleate boiling region, A-B and B-C corresponds to two different flow regimes. The A-B region is featured with isolated bubbles forming at nucleation sites and departing from the surface. Considerable fluid mixing near the surface causes a steep increase in the slope of the boiling curve. As a result, the heat transfer coefficient (h) increases substantially in this region. As surface temperature T_s increases beyond T_B , more nucleation sites become active and increased bubble formation causes bubble coalescence in the vertical direction. The B-C region is characteristic of bubbles escaping as jets or columns. However, as the bubble frequency increases with heat flux, they coalesce in the lateral direction, inhibiting the liquid to contact the heater surface. At point C, q'' ceases to increase and reaches a maximum value termed the critical heat flux (CHF). At this point, a vapor film is formed forcing heater surface to dry out.

Region C-D corresponds to Transition Boiling, during which a vapor film begins to form rapidly on the surface owing to rapid bubble formation. This region is generally studied in a temperature-controlled system as against a heat flux controlled system. This region features a decrease in q'' with increasing wall superheats, since the thermal conductivity of the vapor is much less than that of liquid. Film boiling starts after Point D which is referred

as the Leidenfrost point. The heating surface is completely covered by a vapor film and heat flux is a minimum. As T_s continues to increase, radiation through the vapor film plays a significant role along with conduction through the film. Heat flux continues to increase with increasing wall superheat. Eventually, the excessive heat causes thermal meltdown of the system.

1.3. The Need for Enhancement

In summary, the nucleate boiling region is featured with high heat flux and h at small wall superheats. It is desirable to operate many high power generation devices in this region to exploit the benefits of boiling phenomenon. However, the boiling process is limited by CHF which results in material degradation and thermal meltdown of the system. It can also be noted that adverse effect of heating the chip could occur once the system reaches CHF since the heat transfer of pool boiling is severely limited in the film boiling region.

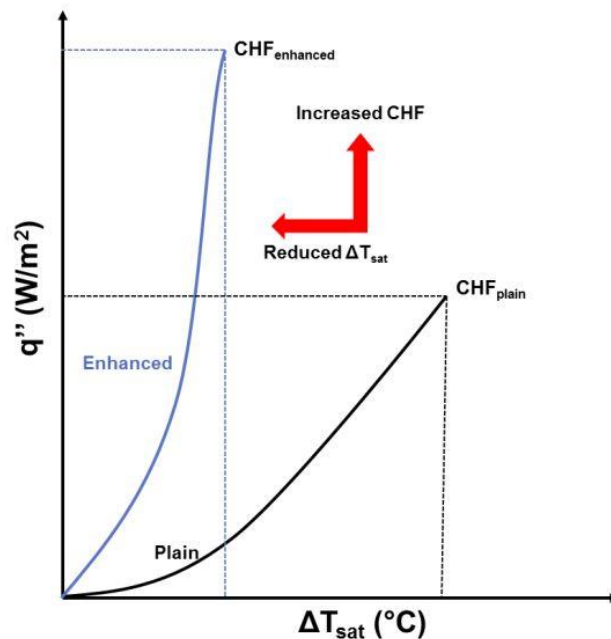
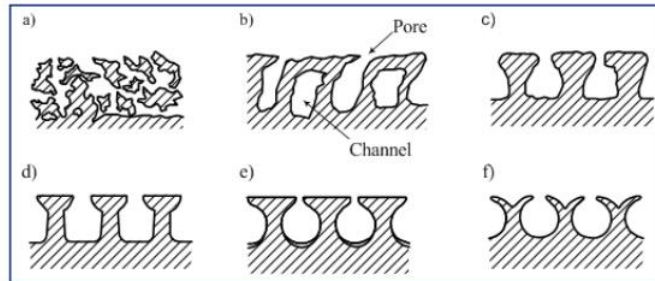


Fig. 3 Pictorial Representation of Boiling Enhancement

While pool boiling on a plain surface yields high heat flux and h at small wall superheats, it will not suffice emerging demand for effective thermal management which requires much higher heat dissipation ability. Consequently, a genuine and challenging need for enhancing boiling heat transfer arises. As shown in Fig. 3, the objective is to (i) increase CHF and (ii) reduce wall superheat.

1.4. *Micro-structured Surface Enhancement for Boiling*

There are generally two methods of boiling heat transfer enhancement – active and passive methods [4]. While heat transfer can be enhanced through active methods such as vibrating or rotating the heating surface, application of an electrostatic field etc., the machinery involved will increase the bulk of the system, making it impractical for chip cooling applications by adversely affecting packing density. Passive methods such as employing special surface geometries have gained a lot of popularity due to its relative simplicity and effectiveness in enhancing pool boiling performance. Fig.4 shows several ways of preparing such surfaces geometries. Literature has shown that microporous /porous surfaces [5–8] have significantly improved the heat transfer performance. Before going into the detailed literature review, the concept of porous surface is introduced.



a) Porous layers made of sintered metal particles from 10 to 100 μm in diameter – High Flux (formerly of Union Carbide and now belonging to UOP); b) Deformed finned tubes with cut and bent over edges, with pore diameters of approximately 100 μm – Thermoexcel-E (Hitachi); c) Knurled and compressed fins – Turbo-B (Wolverine Tube); d), e) and f) Split and compressed fins: d) Gewa-T; e) Gewa-TX; f) Gewa-TXY (Wieland-Werke)

Fig. 4 Micro-Structured Surfaces [4]

1.5. Porous Surfaces

A porous surface is a layer of material containing cavities, channels, or interstices which are typically filled with liquid or gas. The skeletal portion of the material is often called the “matrix”. As seen in Fig. 5, there are mainly three kinds of pore present in the matrix. In region (a) the pores are isolated from the surrounding environment and inaccessible for gas/fluid flow. In region (b), pores are dead-ended but open to surrounding environment. In region (c), pores are open to the surrounding environment and interconnected within the matrix through channels. Additionally, these pores can induce capillary wicking, forming internal liquid path ways in the matrix. The porous surface is often characterized by its material particle sizes, coating thickness, porosity and wickability.

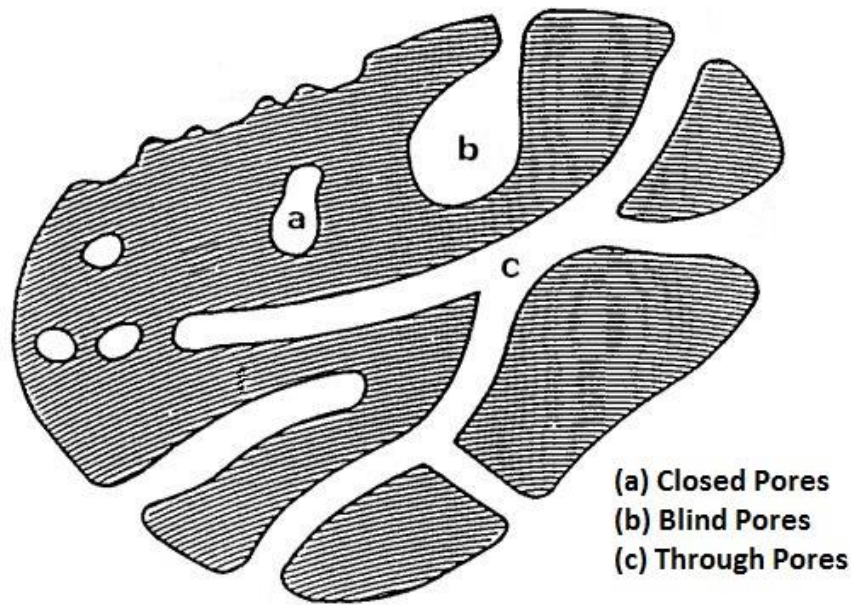


Fig. 5 Schematic cross-section of a porous solid

To be effectively tested under pool boiling environment, the bonding strength of the porous material must be strong enough to prevent lift off. A tape test is typically used to examine how well the material is bonded to the substrate. The porous material must be insoluble in the working fluid. It should be physically and chemically stable in elevated temperatures. Additionally, it should be thermally conductive to transfer heat effectively through the porous matrix. Patil and Kandlikar [5] reviewed several ways of manufacturing porous surfaces such as sintering using metal powders and wire meshes, and electroplating using different chemical bathes. In their comprehensive review, they listed sintering as an efficient and industry-established process used to bond porous particles onto bulk substrates (heat exchangers). Therefore, we identified sintering as an effective technique

to bond the porous material onto our test sections. The process and application of sintering on porous surface will be further discussed in the literature review section.

Chapter 2 **Literature Review**

This chapter summarizes the studies conducted with porous surfaces. The focus of this section are to review the manufacturing and coating techniques, performance characteristics with porous coatings, and mechanisms proposed for enhancing boiling heat transfer.

2.1. Sintering Process

Sintering is a process in which powders are heated at appropriate temperatures, pressures and in appropriate atmosphere to produce a coherent, predominantly solid structure. The produced matrix provides higher surface area to volume ratio compared to its bulk counterparts. Mass transport events often occur on the atomic scale to create bonding which leads to improved strength and lower system energy. Fig. 6 shows the bonding formed between 26 *um* bronze particles sintered at 800 °C under Scanning Electron Microscope. Necks grow between the contacting spheres to produce bonding. As sintering time increases, the degree of necking also increases to provide larger bonding strength.

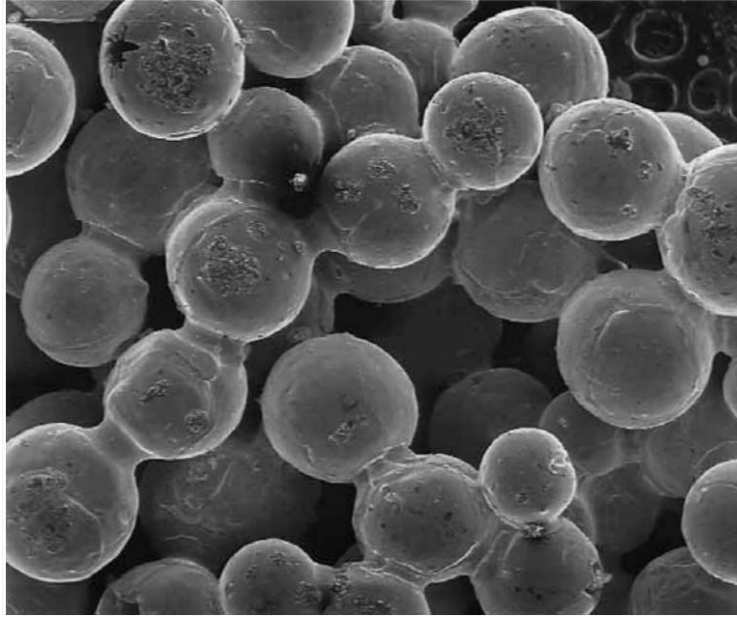


Fig. 6 Scanning Electron Microscopic Images of the Sintering Neck Formation [9]

Sintering process is also an irreversible event which happens in stages, as illustrated in Fig.7. The process begins with loose powders with a certain natural packing density if there is no compression involved. In the initial stage, necks between contacting particles grow to the point where the neck size is less than one-third of the particle size. During the intermediate stage, as necking continues to form among contacting particles, tubular pores form and are connected to external surface. Finally, the degree of necking reaches to a point where there is little porosity left in the material. Pores are closed to the external surface. Grain boundaries eventually develop at these necked regions. As seen in Fig. 7, porosity is an inherent property during sintering process and can be influenced by sintering time.

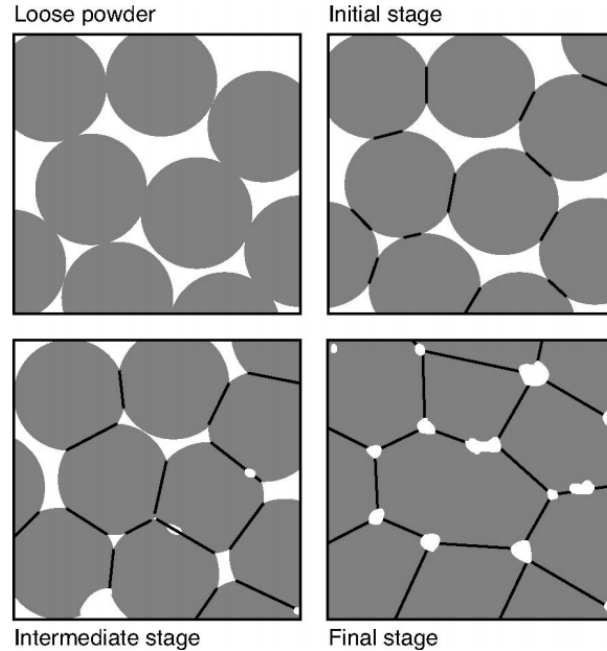


Fig. 7 Illustration of the sintering stages with a focus on the changes in porosity [9]

Here are the definitions of several terms which are critical to sintering process.

- (1) Sintering temperature: The highest temperature during sintering process.
- (2) Sintering time: The time duration for sintering at the highest sintering temperature.
- (3) Sintering Atmosphere: The inert gas used during sintering process to prevent contamination such as oxidation.
- (4) Sintering Pressure: The pressure of the atmosphere in which sintering takes place

2.2. Sintering as manufacturing techniques for porous surfaces

Zhao et al. [10] worked on a lost carbonate sintering process for manufacturing open cell metal foams. They were able to manufacture Copper foams with porosity in the range of 50 – 85 % and cell sizes in the range 53 – 1500 μm . Copper powders and potassium

carbonate mixture was blended, compacted and sintered. The potassium carbonate was removed using either dissolution, melting or other decomposition methods.

Hanlon and Ma [11] fabricated porous surfaces by sintering copper particles (100 Mesh,99.99%) at 840 C and for 12-45 minutes. To isolate the thickness effect, the thickness of the porous surface was decreased by removing layers of the sintered copper particles to allow for subsequent testing.

Table 1 Comparison of Sintering Process Used to Create Porous Surface

Authors [Reference] (Year)	Sintering Parameters	Sintering Findings
Zhao et al [10] (2005)	Particle size of both metal and carbonate particles, Mixing ratio, Sintering temperature and time	Lost carbonate sintering process is a feasible way of producing porous media
Ahmed et al [12] (2007)	The amount of filler material, its type, Sintering temperature, Sintering time, and the pressure of compaction	The amount of filler material could be recognized as the most effective parameter during preparation of porous copper compacts.
Li et al [13] (2010)	Sintering temperature, Sintering time	Sintering temperature and time were found to have an impact on sintering properties and heat transfer properties of sintered wick. The former has a larger impact
Mao-Yu Wen et al [14] (2012)	Sintering pressure, Sintering temperature, sintering time, heating rate, and Particle size	All the chosen parameters have significant effects on pool boiling heat transfer coefficient

Li et al. [15] manufactured porous surfaces by using a multilayered sintered isotropic copper mesh section. The layers of the mesh were first sintered together to obtain desired porosity and thickness. Then the mesh was cut down to desired size and sintered to other components. An optimal sintering process was established to sinter the test sample at 1030 °C in a gas mixture consisting of 75% argon and 25 % hydrogen for two hours. The process

was found to reduce the contact resistance between the sintered mesh and the top surface of the heat source.


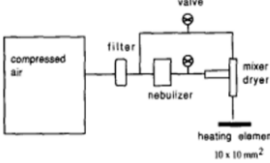

Ahmed et al. [12] used design of experiment technique to investigate the effects of the sintering parameters on the total porosity in the porous surface. The authors identified the amount of filler material, type of filler material, sintering temperature, sintering time and the pressure of compaction were the most important parameters.

In summary, literature has shown that sintering is a feasible process to create porous surfaces. Parameters such as sintering time, temperature, and filler material can be controlled to change morphology and porosity of the surface. Coating techniques which provide methods to coating the sintering material on the substrate is discussed next.

2.3. Coating Techniques

There are several techniques to coat materials onto a flat substrate. As shown in Table 1. Tuma [16] used screen printing technique to apply L-20227 copper powder mixed with Dow 704 silicone diffusion oil on a circular flat Cu disk. The coating thickness ranged from 100 μm to 300 μm . The mesh screen used is Sefar 45-180 mesh polyester screen. The key parameter for controlling coating thickness is the size of the mesh and % weight of the ink vehicle.

Table 2 Comparison of Coating Techniques

Authors [Reference]	Colloidal Solution	Coating Techniques	Targeted Thickness	Illustrations
Tuma [16]	L-20227 Particles (10 μm) mixed with Dow 704 Silicon Diffusion Pump Oil	Standard Screen Printing Technique Using a 45-180 Mesh Screen	100 μm to 300 μm	
Chang and You [17]	Aluminum, Copper, and Diamond with Brushable ceramic and MEK. Diamond with Omegabond 101 and Alcohol, Silver with Omegabond 101 and Alcohol	Spray technique using nebulizer	30 μm to 250 μm	
Chang and You [17]	Aluminum, Copper, and Diamond with Brushable ceramic and MEK. Diamond with Omegabond 101 and Alcohol, Silver with Omegabond 101 and Alcohol	Drip Coating technique using a brush	30 μm to 250 μm	

Chang and You [17] successfully used both spray and drop coating techniques to coat variety of metal particles on horizontal flat surface. For the spray technique, compressed

air at 4 atm was used to apply coating on both flat surface and cylindrical surface. The parameters affecting the coating thickness was the spraying time and the distance between the jet exit and the target surface. Coatings as thin as 30 μm was successfully manufactured using both techniques. Drop coating appears to be the easiest technique to apply metal coating on a flat surface with minimal waste.

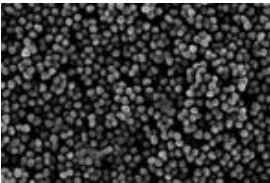
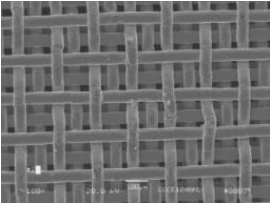
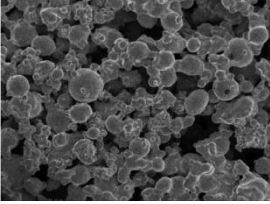
2.4. Pool Boiling Performance Characteristics with Porous Surfaces and Water as Working Fluid

Table 3 summarizes some several pool boiling works with porous surfaces in distilled water. Yao and Kandlikar [18] developed a new technique using electrochemical deposition to directly grow copper nanowires on Si, Au, and Cu substrates. Pool boiling study was conducted on the nanowire structures and results showed significant enhancement over plain copper surfaces.

Li and Peterson [19] systematically investigated the geometric dimension effects (i.e. coating thickness, volumetric porosity, and pore size, as well as the surface conditions of the porous coatings) on pool boiling performance and characteristics on sintered copper mesh surface. Saturated distilled water was used as working fluid and the experiments were conducted at atmospheric pressure. To study the effect of thickness of microporous coated surfaces, a set of experiments were performed on coating thicknesses ranging from 210 μm to 2300 μm while the volumetric porosity (give the value here) and mesh size (value here) of the capillary wick were held constant. All of the samples showed significant enhancement over the plain surface. As thickness of the sample increase, CHF were observed to increase along with increasing wall superheat. Furthermore, the similar studies

were done to study the effects of pore size and particle sizes. While confirming the enhancement effect of porous surface, the authors proposed that both the pore size and the thickness of the porous coating has an effect on boiling incipience superheat. In addition, the authors indicated that thin porous coatings used in the experiments (210 to 570 μm) have large range of heat flux (from 0 to 210 W/cm^2) and at the same time, within a much narrower wall superheat. Hence, boiling heat transfer with thin coatings is suitable for applications for precise temperature control.

Table 3 Comparison of Pool Boiling Studies Using Water At Atm Pressure

Authors [Reference] (Year)	Porous Media (Specific size [μm], coating thickness [μm], porosity [%])	Highest Heat Flux	Highest Heat Transfer Coefficient	Best Performance	Porous Surfaces SEM Images
Yao et al. [20] (2011)	Copper Nanowire (-,5-10,-)	160 W/cm^2 at 11 K (130% Enhancement over plain surface 120 W/cm^2 at 18 K)	145000 $\text{W}/\text{m}^2\text{K}$ (240 % Enhancement Over Plain surface 60000 $\text{W}/\text{m}^2\text{K}$)	160 W/cm^2 at 11 K	
Li and Peterson [19](2007)	Multilayered sintered isotropic copper mesh (56 - 191 Wire dia, 210 - 380, 40.9 - 73.7)	350 W/cm^2 at 65 $^{\circ}\text{C}$ (230 % Enhancement over plain surface 150 W/cm^2 at 25 $^{\circ}\text{C}$)	160000 $\text{W}/\text{m}^2\text{K}$ (260 % Enhancement Over Plain surface 60000 $\text{W}/\text{m}^2\text{K}$)	210 W/cm^2 at 12 $^{\circ}\text{C}$	
Pivovar [7] (2009)	Brazed High Temperature Microporous Coating (4 - 285, 180 - 660, -)	249 W/cm^2 at 35 $^{\circ}\text{C}$ (300 % Enhancement over plain surface 81 W/cm^2 at 20 $^{\circ}\text{C}$)	160000 $\text{W}/\text{m}^2\text{K}$ (400 % Enhancement Over Plain surface 40000 $\text{W}/\text{m}^2\text{K}$)	115 W/cm^2 at 10 $^{\circ}\text{C}$	

Pivovar [7] studied the effect of coating thickness in pool boiling enhancement with brazed High Temperature Microporous Coating. Apparent contact angles and wicking flow rates were measured and found to correlate with pool boiling performance. The author proposed that the CHF with porous materials is found to depend on the coating thickness and wicking flow rate.

McHale et al. [21] compared pool boiling performance of smooth and sintered copper surfaces with and without carbon nanotubes. Pool boiling experiments were conducted in hydrofluorother, HFE-7300, and deionized water. The experimental results in deionized water indicated that the sintered porous surfaces exhibit better boiling performance (lower wall super heat) for lower heat fluxes.

2.5. Mechanism for boiling heat transfer enhancement

There have been extensive investigations to study the mechanisms behind pool boiling with porous surfaces. Mechanically manufactured structured surfaces and porous surface are considered to contain reentrant cavities which are stable vapor traps. [22]. Based on their experiments, Bergles and Chyu [23] confirmed that nucleation takes place within the porous matrix from reentrant cavities (Fig.8). There are preferential vapor escape channels in the matrix which receives liquid supply from surrounded channels. Bubble grows due to evaporation taken place both at the mouth of these channels and inside the matrix where the surfaces are wetted by the liquid. The bubbles are eventually forced out of the surface.

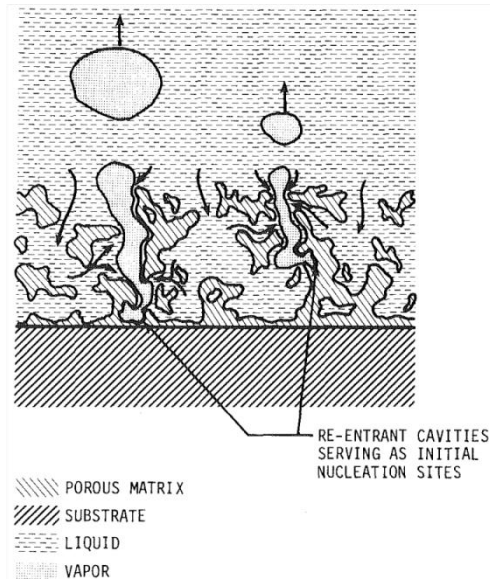


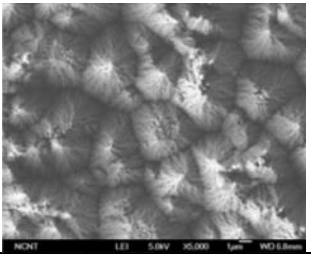
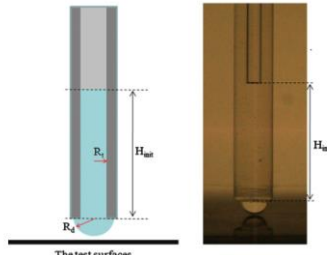
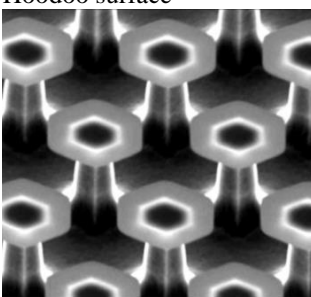
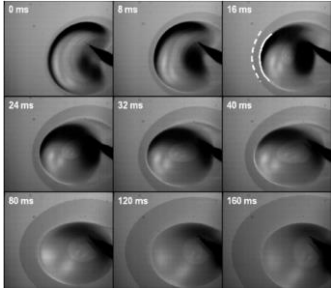
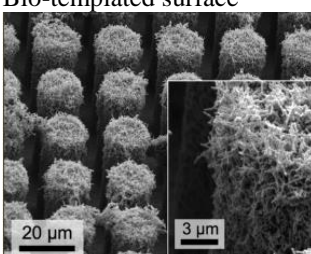
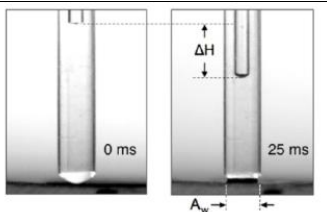
Fig. 8 Proposed Mechanism for Pool Boiling Enhancement with Porous Surfaces (Reproduced from [23])

Kim et al. [8] conducted pool boiling studies with a plain and microporous (Thickness $\approx 50 \mu\text{m}$, Particle diameters in the range of $0.1 - 20 \mu\text{m}$) coated $390 \mu\text{m}$ diameter platinum wire in FC-72. Using “Consecutive Photo Method”, high-speed photos were taken to compare boiling behaviors for both wires and average bubble departure diameters, frequencies, and vapor volume flow rate were also measured at four different nucleate boiling heat flux levels ($6, 11, 13, \text{ and } 16 \text{ W/cm}^2$) using image processing software. The authors proposed that pool boiling enhancement with microporous surface is a direct result of higher nucleation site density. At low heat fluxes, high nucleation site density produces more latent heat contribution. At high heat fluxes, high nucleation site density promotes convection heat transfer with reduced bubble diameters and higher frequencies. Critical Heat Flux is also enhanced as a result of increasing convection heat transfer contribution at high fluxes.

2.6. Effect of Wickability on Pool Boiling Performance

Several microstructure surfaces are found to be super hydrophilic with characteristic contact angle approaching to zero. Studies have shown that these surfaces further enhance CHF due to high capillary wickability. O’Hanley et al. [24] found that the porous hydrophilic surface enhanced CHF by 50% - 60% and hypothesize that the capillary wicking within the pores delays CHF by pulling more liquid into the pores. Table 4 summarized several methods that have been used to characterize wickability.

Table 4 Wicking Characterization Methods of Micro Structured Surfaces

Authors [Years]	Wicking Structures	Wicking Characterization	Schematics
Ahn et al. [25] [2012]	Zirconium surface 	Rate of decrease in capillary height of a pensile water droplet during wicking	 The test surfaces
Bon et al [26]. [2013]	Hoodoo surface 	Wicking front speed based on droplet spreading	
Rahman et al. [27][2014]	Bio-templated surface 	wicked volume flux based on decrease in capillary height during wicking	

Ahn et al [25] studied pool boiling performance using test surfaces made of zirconium alloy. Micro/nanostructure surfaces were created via an anodic oxidation process. The wickability was characterized by measuring the decrease in capillary height over time as a pensile water droplet touched the surface. The micro/nano structured surface was found to have highest wickability and a clear CHF enhancement comparing to bare surface was seen.

Bon et al. [26] studied pool boiling performance of the hoodoo surfaces with various size and spacing. Droplet spreading studies was conducted by measuring wicking front speeds as the droplet in contact with the surface spreads out. The Results proposed that the hemi wicking properties of the surface is the primary mechanism for CHF enhancement.

Rahman et al. [27] studied pool boiling performance of super hydrophilic surfaces using biological templates. Wicking was characterized by calculating wicked volume flux that is based on the rate of decrease in capillary height as a pensile water droplet touched the surface. The author concluded that the wickability can be a single factor in dictating CHF on super hydrophilic surfaces.

2.7. Scope of Work

As seen from literature review, boiling heat transfer enhancement and the proposed mechanisms for porous surfaces make it a potential candidate for high heat flux applications. Wickability characterization of porous surfaces can provide insight in its CHF enhancement. This work primarily focuses on investigating pool boiling heat transfer enhancement of sintered copper porous surface using distilled water as working fluid at atmospheric pressure. Commercial Microporous Metallic Boiling Enhancement Coating (3M Copper Powder) are being used to facilitate easy transfer of process into industries. This study is different from other previous works where the objective is to simultaneously enhance both CHF and h .

In detail, different coating techniques and sintering processes will first be developed to deposit 3M copper powder onto copper substrate. Enhancement in pool boiling performance will be investigated to study the effect of coating thickness and the role of wickability of copper porous surface on CHF. It's hard to observe pool boiling due to its chaotic nature at high fluxes. Visualization research will be conducted using high speed images to obtain further insight on enhancement mechanisms.

Chapter 3 **Experimental Work**

The experimental work consists of two-part study. Part I of the study focused on the effect of coating thickness on pool boiling performance of sintered porous surfaces using drop coating technique. Part II of the study explored the same coating thickness effect using screen printing technique which produces surface with better thickness uniformity. The role of wickability on CHF enhancement was studied and visualization research provided insight into the pool boiling enhancement mechanism.

3.1. Sintering Process Set Up

The deposition of the copper coating in this work is done using a sintering process (Fig.9) to fuse copper particles into the copper substrate. Hence a tube furnace (Lindberg/Blue Mini-Mite™) is used to heat the sample up to high temperatures ranging 800 – 1000 °C. Fig.9 shows detailed schematics of the process. Two needle valves are installed on both sides of the furnace for leakage troubleshooting and flow regulating. In addition, a flow meter (FMA 1700 Omega) is installed at the inlet of the furnace to measure the flow rate of the purging gas. At the outlet of the furnace, a mechanical pressure gauge is installed to measure the vacuum pressure in case the sintering is taken place under vacuum. The flow condition can be checked by observing bubbles in the beaker and the exhaust gas is evacuated through a fume hood. Test samples are loaded into the tube at the inlet of the furnace. They are located at the center of the tube to receive uniform heating. For present work, Helium is used as purging gas. Forming gas which consists of hydrogen and nitrogen is typically used as sintering atmosphere. However, it is not readily feasible during preliminary work due to added complexity and safety concern for hydrogen gas.

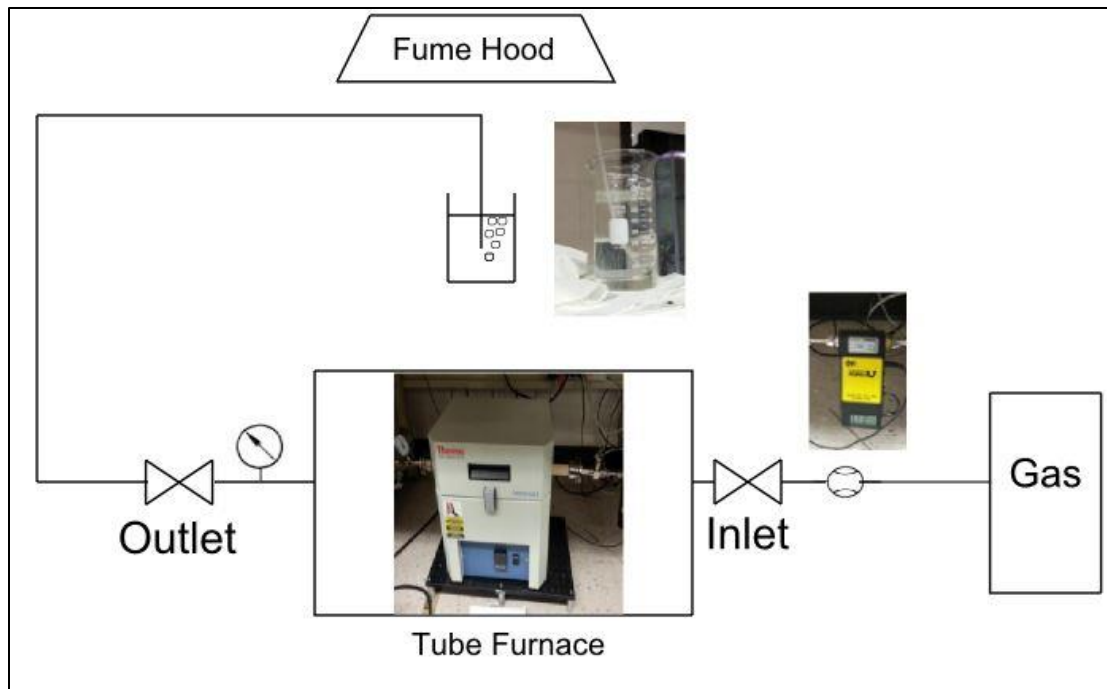


Fig. 9 Sintering Set Up

3.2. Test Set Up

The pool boiling test set up consists of heater assembly, test sample holder assembly, the glass water bath, height adjustment fixture, water reservoir assembly, and visualization unit (Fig. 10). The heater assembly consisted of heater block machined using copper 101 alloy block. 4 x 400 W cartridge heaters were inserted into the heater block on four side, providing ample heat transfer into the test sample. A 10 mm x 10 mm square pin was machined on the top surface of the heater to ensure consistent 1 cm² contact area with the test sample. Additionally, the contacting two surfaces were surface grinded to improve surface finish and pressed together using Grafoil sheet of the same 1 cm² contact area to minimize contact resistance. The entire heater assembly was suspended on four compression springs to provide uniform contact pressure on the test sample contact surface.

This facilitate 1 D heat conduction from heater to the test surface. The glass water bath provides unobstructed view to study boiling phenomenon. A clear fused Quartz square tube was placed on the top surface of the copper test sample. To prevent water leakage through the edge of the top surface. A thin epoxy layer was applied to affix a 10 mil thick (0.254 mm) Teflon ® gasket on the top surface of the test sample, leaving the 10 mm x 10 mm coating area exposed to water.

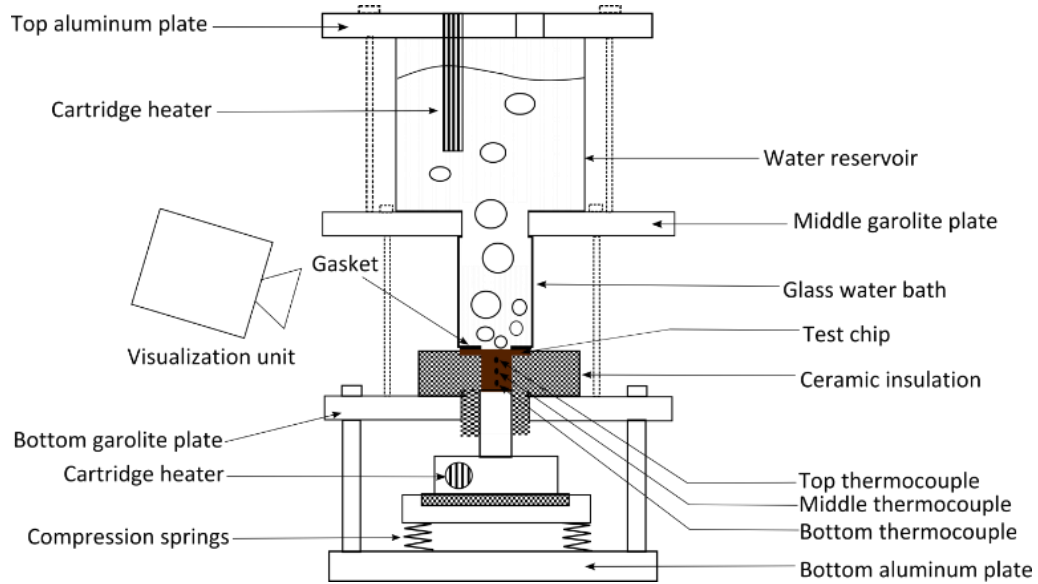


Fig. 10 Pool Boiling Test Set Up

The test sample contains 10 mm x 10 mm porous coating on the top surface. A ceramic holding fixture was installed to hold the test sample in place and to minimize heat lost to the surrounding. The test sample holder assembly was installed on an aluminum plate with alignment shafts installed at four corners. This allowed the test set up assembly to adjust vertically to provide sufficient contact pressure between the 10 mm x 10 mm heat conduction area on the bottom of the test sample and the top surface of the heater surface. Additionally, test sample experiences temperature spike at CHF, the height adjusting

fixture ensure timely separation of the test sample away from the heater to prevent melt down and cracking of the fused Quartz square tube. The water reservoir assembly holds distilled water in a cylindrical chamber. An aluminum plate was fixed on top of the reservoir to prevent water splashing and heat loss to the environment. A hole was drilled on the plate to maintain the reservoir at atmospheric pressure. A submersible Watlow 200 W cartridge heater was used to maintain distilled water in the boiling chamber at saturation temperature.

3.3. Test Samples

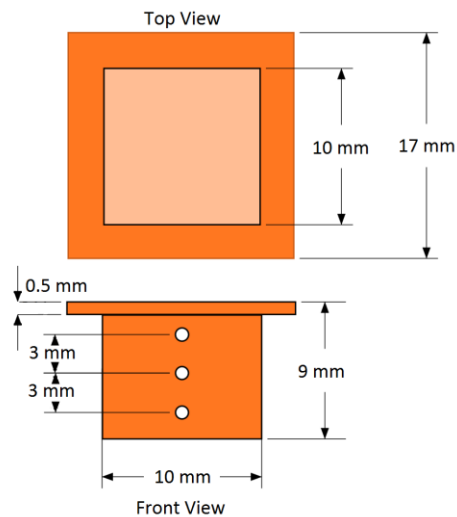


Fig. 11 Test Sample

The test sample was made from copper 101 alloy. In – house CNC Mill was used to machine the sample featuring a base protrusion of 10 mm x 10 mm cross-section area and a top plate of 17 mm x 17mm x 0.5 mm. The square protrusion allows 1-D conduction when contacting the heater surface. Three holes of .635 mm in diameter and 5 mm in depth was drilled into front side of the sample to allow thermocouple (Omegaclad XL K Type)

temperature measurements. The three holes has equal distance of 3 mm apart. The top plate was machined to minimum allowed thickness before the material buckle. This minimized heat loss from the 1-D condition while provides a sealing surface for the glass water bath.

3.4. Pool Boiling Procedure

Procedure of pool boiling test is summarized:

- Mount test sample in the ceramic holder, assemble test set up as shown in Fig. 10
- Fill distilled water in the glass water bath and the reservoir
- Insert 3 x thermocouple (Omegaclad XL K Type) into the thermocouple holes on the front side of the chip.
- Turn on auxiliary cartridge heater in the reservoir to heat and degas the distilled water
- After degassing and distilled water in the bath reached saturation temperature, turn on main power supply. Starting Voltage is about 20 V.
- Wait for steady state condition, then record thermocouple measurements for 10 sec. Then increase power supply voltage by 5 V.
- Repeat the process until the system reaches CHF.
- At CHF, immediately inject cold water at test surface and separate the test sample contact area with the heater surface using the height adjustment fixture.

3.5. Data Analysis

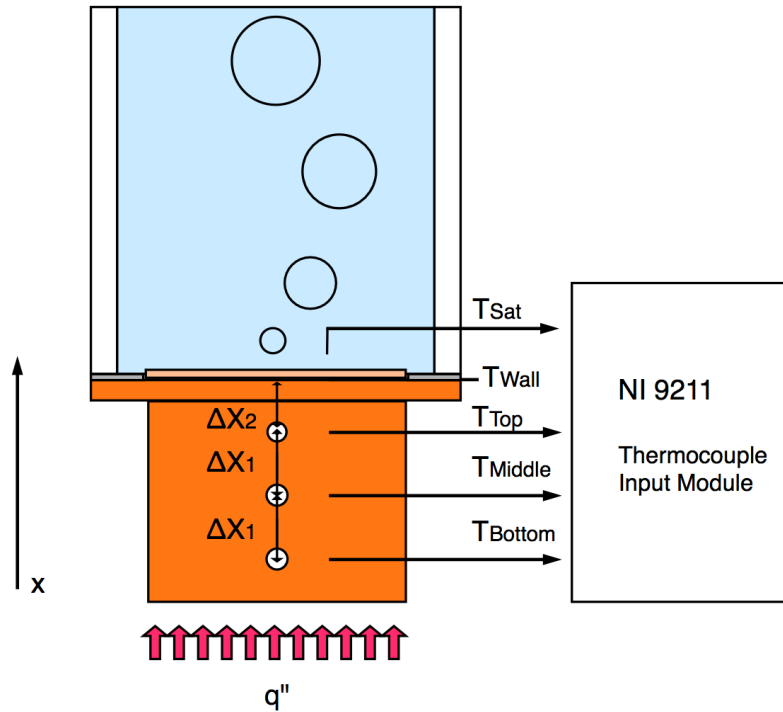


Fig. 12 Schematics for data acquisition

Pool boiling curves involves the calculation of heat flux q'' , heat transfer coefficient h and wall superheat ΔT_{sat} . Thermocouple measurements at T_{Top} , T_{Middle} , and T_{Bottom} , provides a way to measure heat flux going through the test sample using Taylor Series Approximation and 1-D conduction assumption.

Fourier's Law in 1-D form is:

$$q'' = -k_{cu} \frac{dT}{dx} \quad (1)$$

k_{cu} is the thermal conductivity of copper and $\frac{dT}{dx}$ is the temperature gradient in x direction.

Using Taylor Series Approximation, $\frac{dT}{dx}$ can be estimated using thermocouple measurements at top, middle, and bottom locations in the chip and the distance between the thermocouples ΔX_1 . (Fig. 12)

$$\frac{dT}{dx} = \frac{3T_{Top} - 4T_{Middle} + T_{Bottom}}{2\Delta X_1} \quad (2)$$

Wall superheat $\Delta T_{sat} = T_W - T_{Sat}$

T_W is temperature at the top surface of the test sample where bubble nucleation happens.

$$T_W = T_{Top} - q'' \frac{\Delta X_2}{k_{cu}} \quad (3)$$

ΔX_2 is the distance between the top thermocouple hole and the top of the test surface.

T_{sat} is the saturation temperature of water, measured by thermocouple.

Heat transfer coefficient h is calculated by:

$$h = \frac{q''}{\Delta T_{sat}} \quad (4)$$

As shown in Fig. 12, all thermocouple data were logged using NI 9211 Thermocouple input module and calculated heat flux, heat transfer coefficient and wall superheat values were recorded using a customized Labview VI.

3.6. Uncertainty Analysis

Uncertainty of the pool boiling results were analyzed using Equation (5)

$$U_y = \sqrt{B_y^2 + P_y^2} \quad (5)$$

Where the U_y is the uncertainty of a parameter y; B_y is the bias errors which can be fixed or systematic. Sources of bias error can come from calibration errors of a measurement system and loading errors if the system is intrusive. Precision error P_y is random errors caused by lack of repeatability in the output of the measuring system. Sources of precision error can come from uncontrolled variables in the measurement process. Table 5 shows the sources of precision errors associated with the pool boiling experiments such as thermocouple calibrations, thermal conductivity of copper and the machining tolerance of the test chip.

Table 5 Uncertainty Parameters

Parameter	Value	Units	Precision Error U_y	% Uncertainty
k_{cu}	391	W/m°C	9.00	2
ΔX_1	3.00E-03	m	1.00E-04	3
ΔX_2	1.70E-03	m	1.00E-04	6
T_{Top}	Varies	°C	0.08	Varies
T_{mid}	Varies	°C	0.11	Varies
T_{bottom}	Varies	°C	0.08	Varies

To calculate the uncertainty of heat flux $U_{q''}$, Equation (5) can be further modified into

$$\frac{U_{q''}}{q''} = \sqrt{\left[\left(\frac{U_k}{k}\right)^2 + \left(\left(\frac{3U_{T1}k_{cu}}{\Delta X q''}\right)^2 + \left(\frac{4U_{T2}k_{cu}}{\Delta X q''}\right)^2 + \left(\frac{U_{T3}k_{cu}}{\Delta X q''}\right)^2 + \left(\frac{U_{\Delta X}}{\Delta X}\right)\right]^2} \quad (6)$$

Using the uncertainty values obtained in Table 5, the variation of uncertainty with q'' for three test samples were calculated and plotted in Fig.13. The uncertainty is seen to be decreasing with increasing heat flux. The interest of this study is at high heat flux region

including CHF and the uncertainty is found to be below 6%. Similar calculation was done for h. The uncertainty was found to be below 6% in the same region.

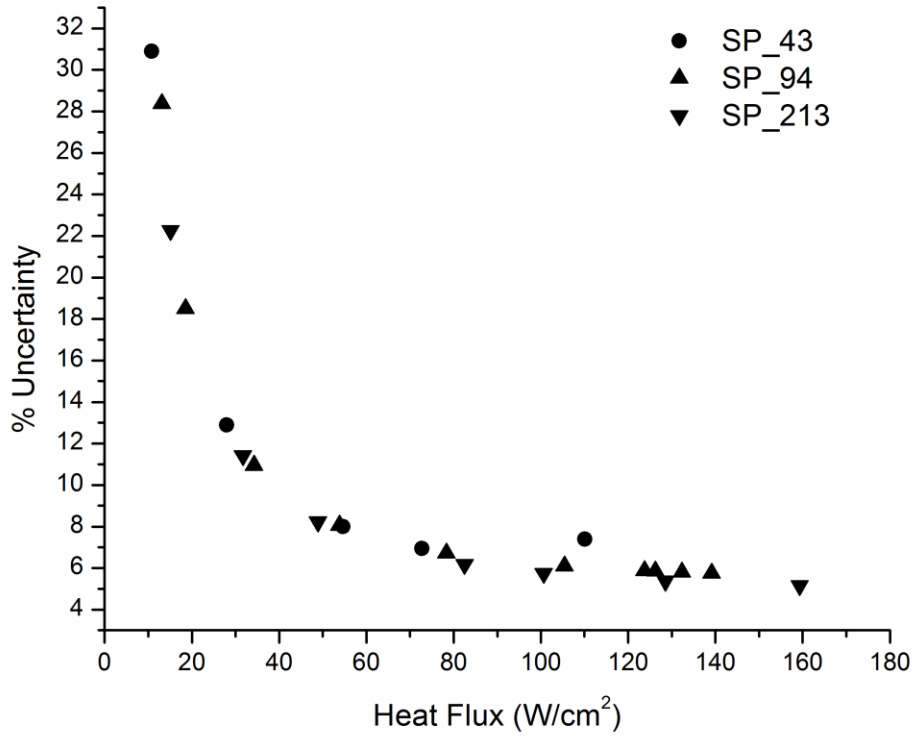


Fig. 13 Uncertainty for Heat Flux

Heat loss study was conducted for a randomly selected test sample. Temperature distribution across the test section was plotted at three heat fluxes. As shown in Fig.14, all temperature profiles shows linear pattern with R squared value closed to 1. This confirmed the 1-D heat conduction assumption used for heat flux calculation and there is minimal heat loss across the test section.

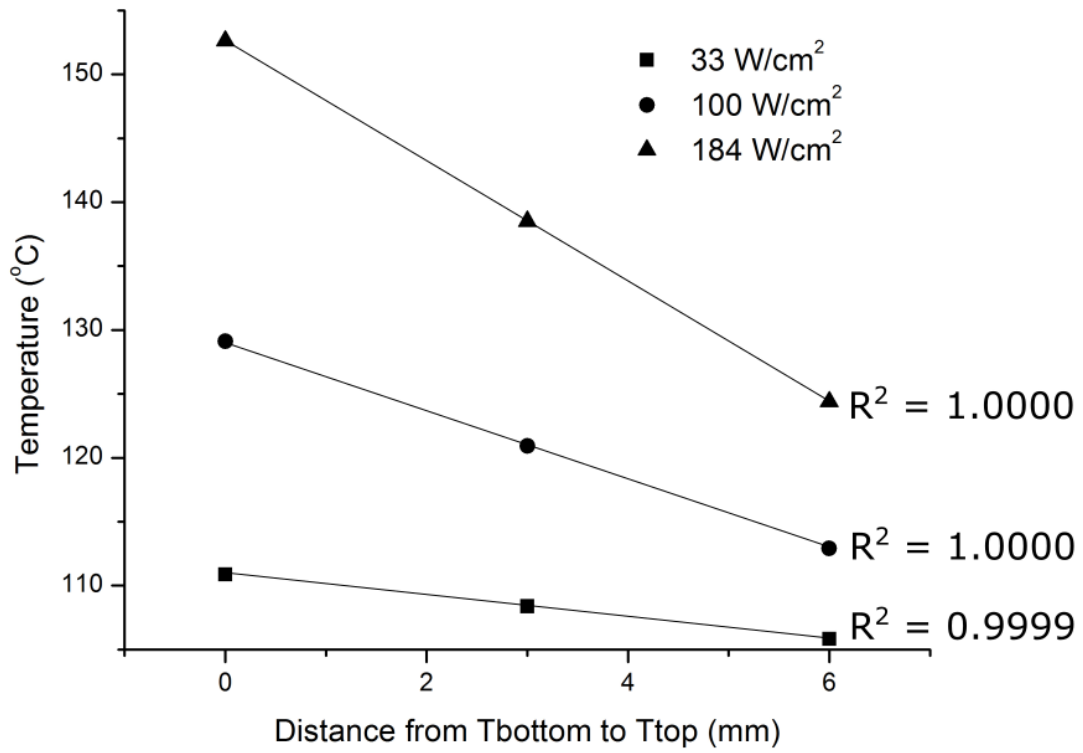


Fig. 14 Heat loss study showing temperature profile in the test sample

3.7. Drop Coating Technique

As seen in literature review, drop coating was used as coating technique for deposition of microporous surfaces owing to its simplicity in application. Therefore, this technique was used in the first part of the study to deposit 3M L-20227 Microporous Metallic Boiling Enhancement Coating on four copper test surfaces. This copper powder was specifically developed by 3M™ for boiling application. The coating thicknesses obtained range from 49 μm to 447 μm as seen in Table 5.

Table 6 Test Matrix for Drop Coating

Chip Label	Dope Casting Solution	Average Coating Thickness (μm)	S.D in Coating Thickness (μm)	Sintering Temperature [°C]	Sintering Time (Hr.)
DC_49	Cu,Na ₂ CO ₃ , IPA	49	14	800	2
DC_97	Cu,Na ₂ CO ₃ , IPA	97	61	800	2
DC_238	Cu,Na ₂ CO ₃ , IPA	238	39	800	2
DC_447	Cu,Na ₂ CO ₃ , IPA	447	13	800	2

As illustrated in Fig.15, a solution mixture consists of 3M copper powder (3M L-20227 Microporous Metallic Boiling Enhancement Coating), Sodium Carbonate and IPA was dropped onto the top surface of a substrate. The mass ratio of copper power, Sodium Carbonate, and IPA was 3:1:1. A pocket of 10 mm x 10 mm x 0.4 mm was machined on the top surface of the chip to contain the droplet from spreading over the entire surface and to provide reference for coating thickness measurement. IPA evaporates at room

temperatures quickly, leaving the copper powder and Sodium Carbonate coating on the substrate surface. Then, coating thickness can be further increased by adding more droplets onto the substrate.

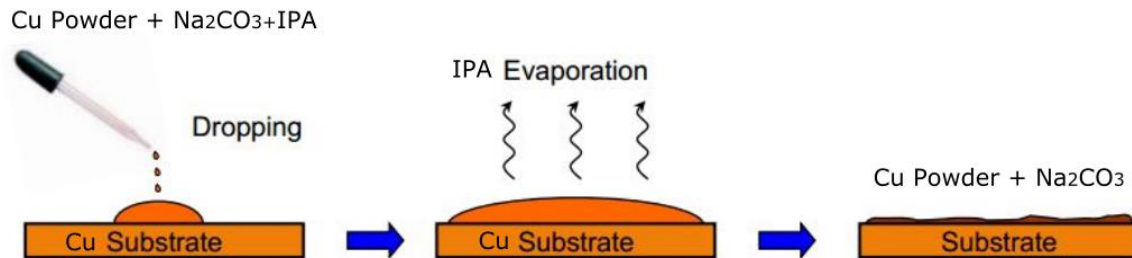


Fig. 15 Drop Coating Technique

3.7.1 Sintering Process

A lost carbonate sintering process similar to the work done by Zhao et al. [10] was used to sinter the 3M copper powder on copper test surface. Preliminary sintering tests were conducted using the 3M copper powder and IPA only at three different sintering temperatures (700 °C, 800 °C, and 900°C). Sintering time was kept the same for 2 Hours. As seen in SEM images at 1000X in Fig. 16, For the surface sintered at 700 °C, clear particles shapes can be seen, suggesting that there was not enough bonding formed between the particles at this temperature. The surface was not suitable for pool boiling application as the surface would break off during intensive agitation caused by bubble nucleation. For the surfaces sintered at 900 °C, the shape of the particles could no longer be recognized suggesting high degree of sintering at this temperature. This was not ideal pool boiling application neither since few open pores and through pores which are essential for nucleation and liquid transport can be found. Therefore, 800 °C and 2 hours was chosen as

sintering recipe for this coating technique since potential open pores and through pores can be found.

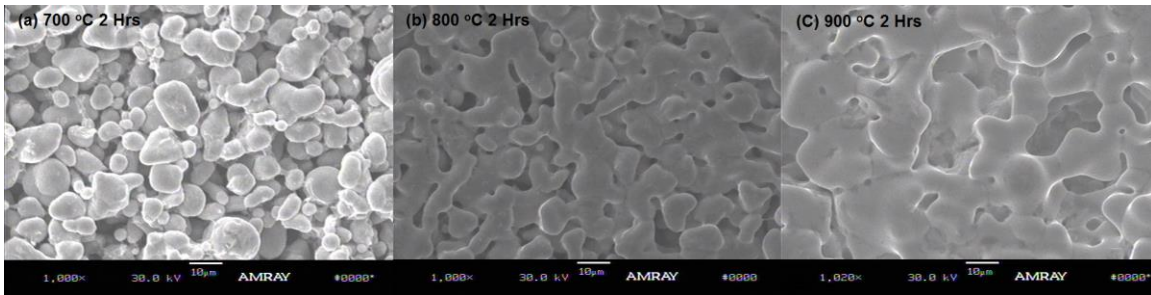


Fig. 16 SEM Images At 1000X Showing Surfaces Sintered At Three Different Temperatures (Equipment: AMRAY 1830)

Furthermore, Sodium Carbonate Na_2CO_3 was used to increase the porosity of the sintered porous surface. Since the melting temperature of Na_2CO_3 is 851 °C. the particles were expected to remain in the matrix at sintering temperature of 800 °C. After sintering, the Na_2CO_3 particles could then be dissolved in an open water bath to increase porosity of the porous surface. Four chips as shown in Table 6 were prepared using this recipe. SEM images (Fig. 17) shows large open pores formed during sintering, suggesting the presence of Na_2CO_3 increased the porosity of the porous matrix.

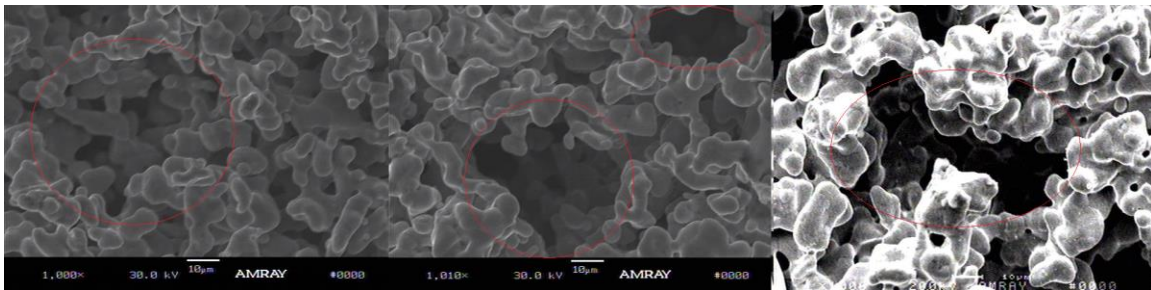


Fig. 17 SEM Image At 1000X Showing Large Pores Formed Using Lost Carbonate Sintering Process (Equipment: AMRAY 1830)

3.7.2 Effect of Coating Thickness on Pool Boiling Performance using Drop Coating Technique

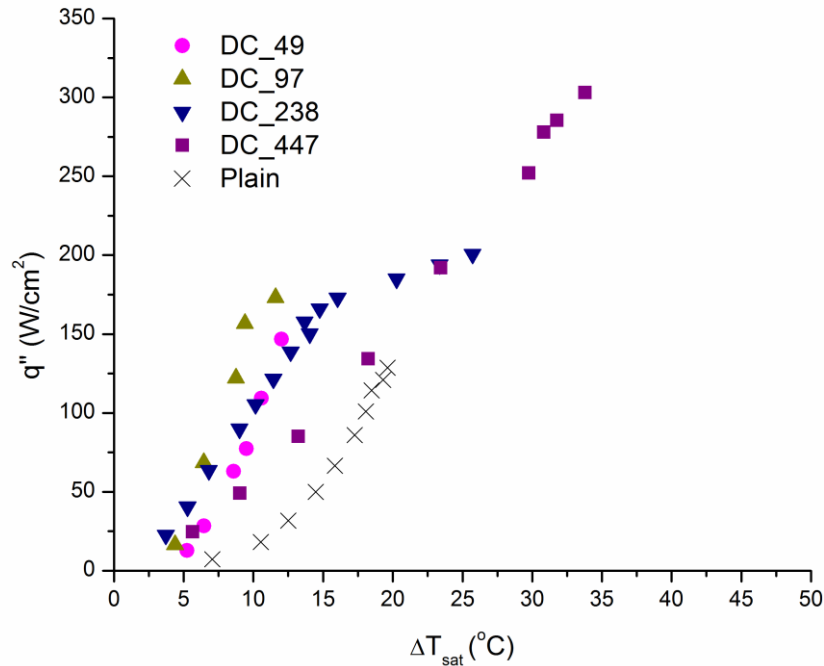


Fig. 18 Pool Boiling Curves using Distilled Water at Atm Pressure for Sintered Porous Surfaces Manufactured By Drop Coating And Lost Carbonate Process

Four test sample prepared according to test matrix in Table 6 were tested for pool boiling performance using distilled water at atmospheric pressure. The pool boiling curves were shown in Fig. 18. As a baseline comparison, test sample with plain surface was first tested and result showed that all porous surfaces show consistent enhancement. The highest CHF was obtained on test sample DC_447 to be $303 \text{ W}/\text{cm}^2$ at wall superheat of $33.8 \text{ }^{\circ}\text{C}$. This is approximately 135 % enhancement over the CHF obtained by a plain surface.

This proved that porous surface enhances pool boiling performances by increasing CHF and reducing wall superheat. This is evident in the leftward shift of the pool boiling curve.

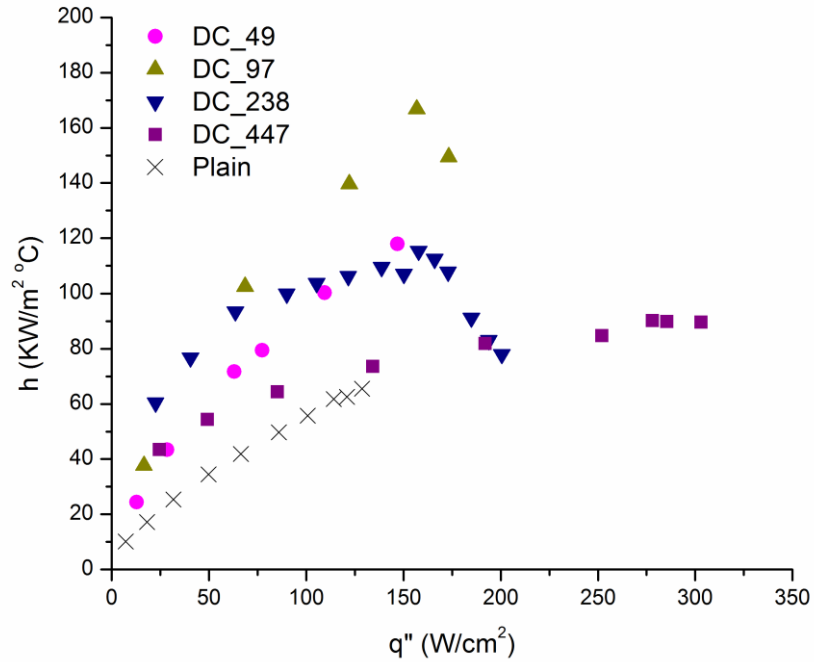


Fig. 19 Variation of Heat Transfer Coefficient h with Heat Flux On Surfaces Using Drop Coating And Lost Carbonate Sintering Process

The variation of heat transfer coefficient h with heat fluxes are plotted in Fig. 19. The highest h was obtained by test sample DC_97 to be 167 kW/m² °C at heat flux of 157 W/cm². It can also be noted that between heat flux of 50 W/cm² and 150 W/cm², thinner coatings generally perform better than thicker coating and plain surface.

The effect of coating thickness on CHF can be seen in Fig. 20. The CHF increased with the increase of the coating thickness. The highest CHF was obtained by test sample DC_447 with the coating thickness of 447 μ m. The result is consistent with literature findings [6,7,28] that coating thickness of a porous surface affects pool boiling performance.

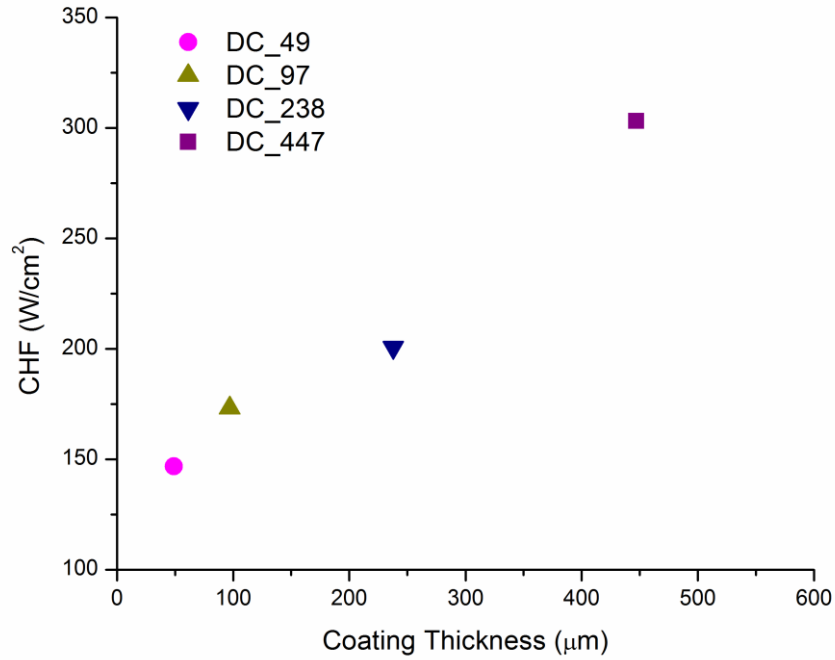


Fig. 20 Effect of Coating Thickness on CHF Drop Coating Technique

One of the issue faced with drop coating technique is that there is poor coating thickness uniformity as seen in Table 6. This is mainly due to the challenge to fully suspend 3M copper powder, Na_2CO_3 in IPA solution. To further study the effect of coating thickness on pool boiling performance, another coating technique with better coating thickness control must be explored. The next section screen printing technique was introduced.

3.8. Screen Printing Technique

Screen printing was used as coating technique to deposit 3M copper power on copper substrate. Fig. 21 shows a schematic of a typical screen printing process. Ink is transferred onto a substrate using squeegee strokes. This forces the ink through a polyester mesh. The mesh is typically stretched on a rigid frame and has opening area which allows the ink to pass through. The open area can be designed to achieve desirable pattern using photo-emulsion method. Two squeegee strokes are usually involved when printing the ink onto a substrate. First squeegee strokes fill the mesh open area with ink. The second stroke uses more force and causes the mesh to touch the substrate. This causes the ink to wet the surface and be pulled out of the mesh as the screen springs back after the stroke finished.

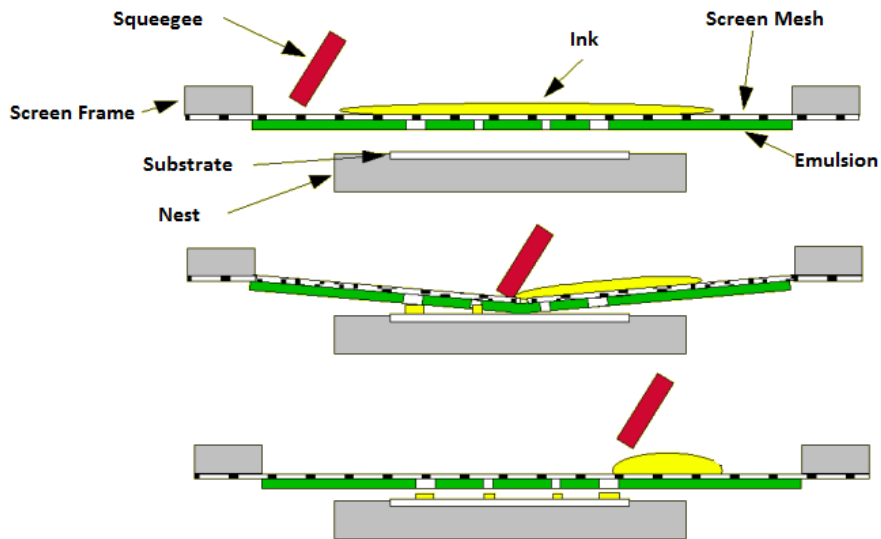


Fig. 21 Schematics of A Typical Screen Printing Process

The ink of choice was Nazdar 9627 overprint clear ink. It is typically used to print a glossy clear layer onto the first layer of colored print. This ink was proven in the industry to successfully deposit metal costings using screen printing. The 3M solution achieved ideal

colloidal suspension using a planetary centrifugal mixer. The working mixing recipe was found to be 2000 PRM for mixing speed and 1 min for total mixing time (max 20 seconds was allowed for each run and cooling time should be allotted for solution between runs). Fig. 22 shows a summary of the manufacturing process developed for this coating technique. The polyester mesh chosen was manufactured by monoprint®. It has 110 mesh count (number of threads per square inch) which is commonly used as an industry standard for a variety of application. Its mesh opening was about 50 μm which has enough clearance for 3M copper powder to pass through. Photo-emulsion method was used by a screen printing company to create a 10 mm x 10 mm opening area on the polyester mesh, this determined the size of the ink deposit on the substrate and the resulting test surface in pool boiling tests.

The thickness of the emulsion was reported to be approximately 35 μm . This roughly determined the coating thickness of the ink deposit. Additional thickness can be added using extra layer of masking tape. Nazdar 9600 series ink dries quickly at 150 F. A pre-sintering drying process (150 F for 2 min) was done in a convection oven so that the shape of the deposit can be maintained after removing the masking tape. The surface after drying can be seen in (b) in Fig. 22.

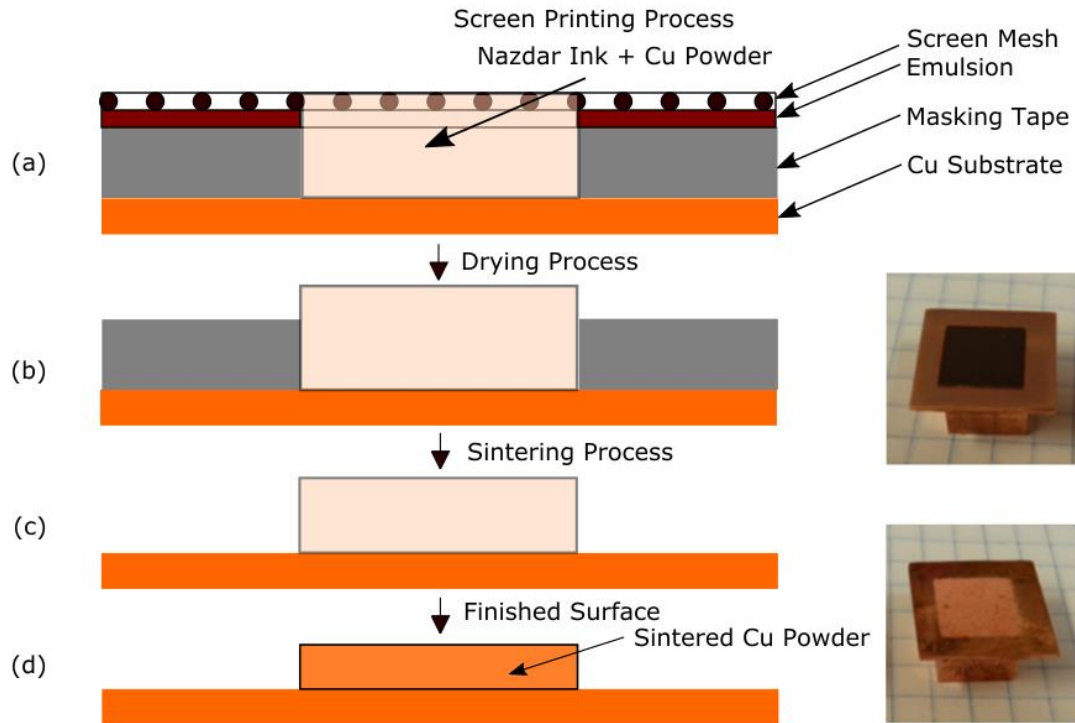


Fig. 22 Summary of Manufacturing Process Using Screen Printing Technique

Thermogravimetric analysis (TGA) was used to determine the sintering recipe for screen printing technique. A sample of the 3M copper power and ink solution was heated in a furnace up to 800 °C in a Nitrogen environment. Mass of the sample was constantly measured. A notable decrease in mass was can be at 200 °C, indicating partial burn-off of the ink constituents. The mass of the sample reached minimum at 400 °C, indicated complete burn-off of the ink constituent. Therefore, an intermediate burn-off process was set at 500°C for half an hour during the sintering process. Fig. 23 shows a summary of the sintering recipe. Purging was done for 1 hour using Helium. Flow rate of Helium was set at 30 ml/min. The furnace then ramped up to 500 °C at 17 °C / min. Then the furnace held at 500 °C for ½ hour. Sintering temperature was set at 850 °C and sintering time was set for 1 hour. After sintering, the furnace powered off and a fan was used for cooling.

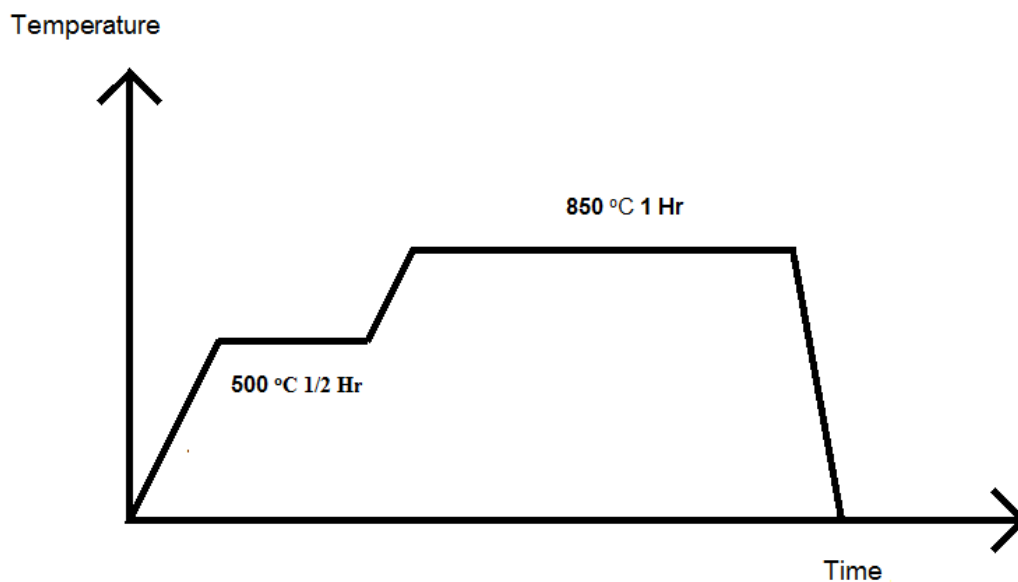


Fig. 23 Sintering Recipe for Screen Printing Technique

Fig. 24 shows the top view of the sintered porous surface and X-Ray Power Diffraction (XRD) result to determine the composition of the sintered material. The edges of the sintered surface were clearly defined by 10 mm x 10 mm opening area on the mesh. It can be seen on the picture that there was consistent deposition on the surface. XRD results determined the main constituent of the material to be copper. These observations confirmed that the screen printing technique can be used to deposit 3M powders on the copper substrate and the sintering recipe successfully removed ink product during the intermediate heating step.

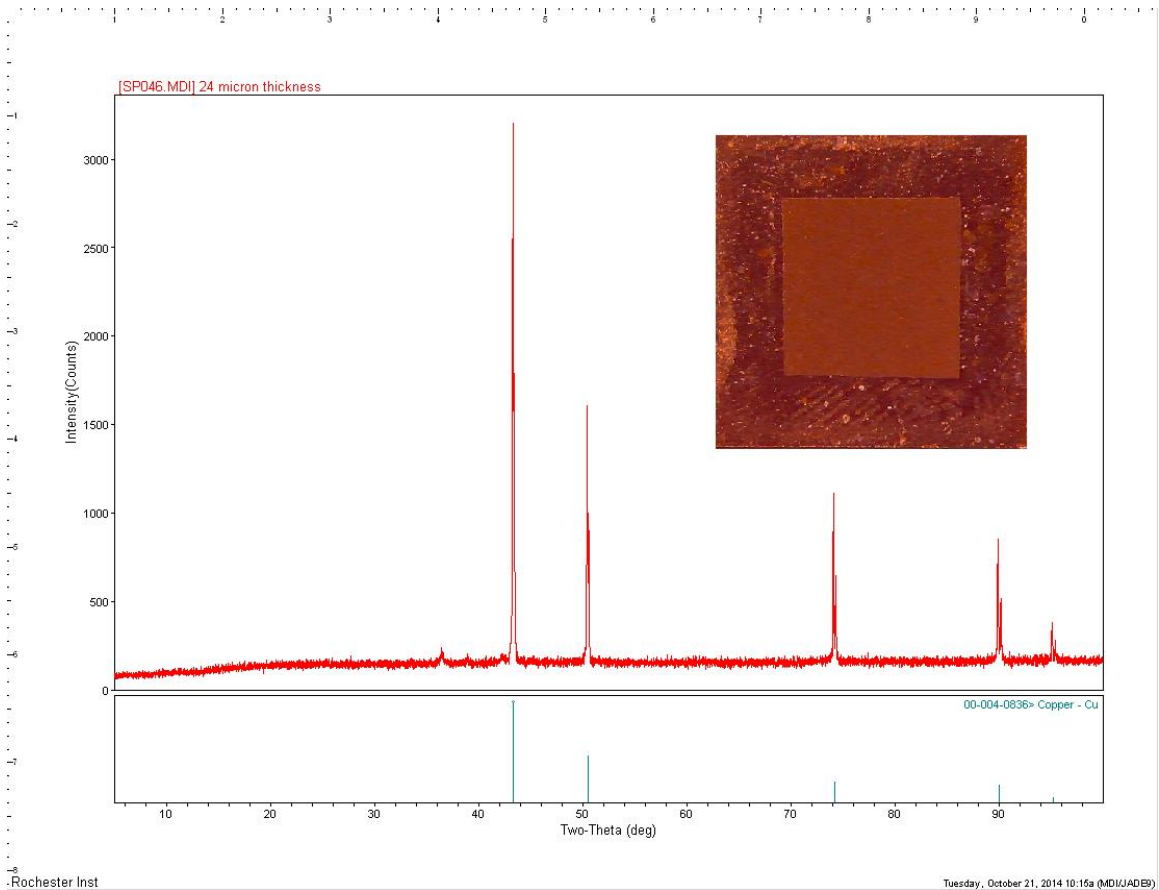


Fig. 24 XRD Results For A Sample Screen Printed Surface After Sintering

3.8.1 Determination of Cu: Ink Mass Ratio

The mass ratio of ink and metallic powder is important in screen printing process. A larger ink percentage in the solution could lead to insufficient deposit and non-uniformity in the finished surface. A larger metallic powder percentage could lead to difficulty in transferring the ink through the mesh. Table 7 shows the test matrix to determine a working ratio for this study. 3M powders were deposited onto test substrate using 3 different Cu to ink mass ratios. Laser Confocal Microscope (LCM) was used to measure the coating thickness and to compare the difference in thickness uniformity. It shall be noted that the

test chip was labeled based on the coating thickness. For example, SP_45 means the test chip final coating thickness after sintering is 45 μm .

Table 7 Cu: Ink Mass Ratio Study

Chip Label	Cu: Ink Mass Ratio	Coating Thickness (μm)	Sintering Temperature ($^{\circ}\text{C}$)	Sintering Time (Hr)
SP_45	2:1	45	850	1
SP_50	1:2	50	850	1
SP_50	1:1	50	850	1

The effect of Cu to Ink Mass Ratio on coating thickness uniformity can be seen in Fig. 25. Laser Confocal Microscope images at 10 X magnification show that Cu to Ink ratios of 1:2 and 1:1 created inconsistent coating with a moon crater type morphology. This inconsistency in thickness is not desired for the current study on the effect of coating thickness on pool boiling performance. On the other hand, a mass ratio of 2:1 created a uniform coating as seen in both 10X and 50X magnification LCM images (Fig. 25 (c)). Hence, this mass ratio is used throughout the study.

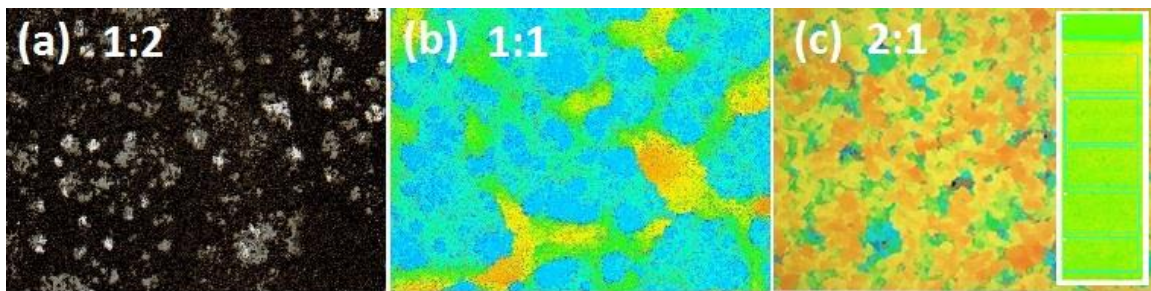


Fig. 25 LCM Images Showing Effect of Cu : Ink Mass Ratio on Morphology (a) SP_50 Cu : Ink 1:2 at 10X Magnification (b) SP_50 Cu : Ink 1:1 at 10X Magnification (c) SP_45 Cu: Ink 2:1 at 50X and 10X Magnification

(Equipment : Keyence)

3.8.2 Effect of Coating Thickness on Pool Boiling Performance using Screen Printing Technique

The purpose of this study is to evaluate screen printing as coating technique to create porous surfaces using 3M copper powder. The effect of coating thickness on CHF is studied to validate the result obtained using drop coating technique. Table 8 shows four test chips used in this study. Cu: Ink mass ratio was kept the same as 2:1. Sintering recipe was 850 °C for 1 Hr.

Table 8 Test Matrix Effect of Coating Thickness

Chip Label	Cu:Ink Mass Ratio	Coating Thickness (μm)	S.D. (μm)	Sintering Temperature (°C)	Sintering Time (Hr)
SP_28	2:1	28	15	850	1
SP_43	2:1	43	6	850	1
SP_94	2:1	94	18	850	1
SP_213	2:1	213	21	850	1

3.8.2.1 Morphology

LCM was used to measure the coating thickness of each test chip. The height difference of multiple locations on the test surface was measured to obtain the standard deviation (S.D). In addition, Fig. 26 shows LCM images for sample test chips of various coating thickness. The screen printing process with Cu: ink mass ratio of 2:1 yielded similar coating uniformity as seen in previous study. It shall be noted that as thickness increased, larger pores were seen on the surface. This can be identified as the dark blue areas on the image.

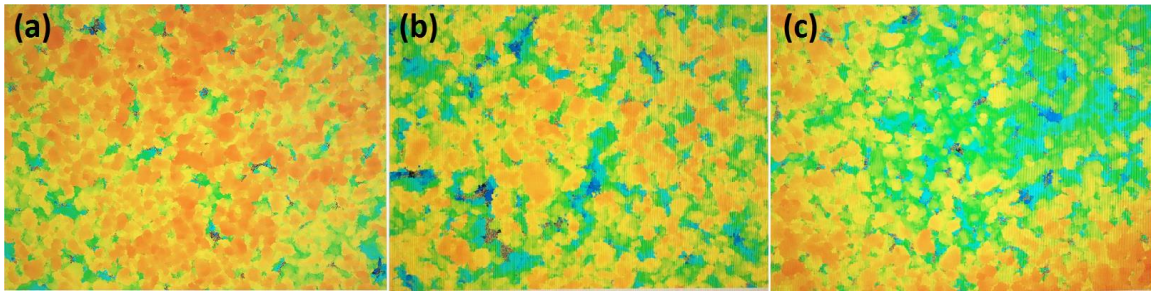


Fig. 26 LCM Images Showing the Thickness Uniformity of Sample Coating at 50X Magnifications (Equipment: Keyence) (a) SP_43 (b) SP_94 (c) SP_213

The degree of sintering and morphology was further studied using AMRAY 1830 scanning electron microscope (SEM) at an accelerating voltage of 30.0 kV. Fig. 27 (a), (b), (c) shows the SEM of 3M copper powder coated on the copper test surface at different thicknesses. At the magnification of 1000X, the coating demonstrated porous structured morphology with open pore diameter as small as 1 μm . Consistent necking can be observed at all SEM images. This confirms that the sintering recipe maintained a uniform degree of sintering across all thicknesses. Furthermore, Fig.27 (d), (e), (f) at magnification of 500X show consistent coating uniformity comparing with LCM images. The surface was uniformly coated using the determined Cu: Ink mass ratio and larger pores were seen for the coating thickness of 213 μm .

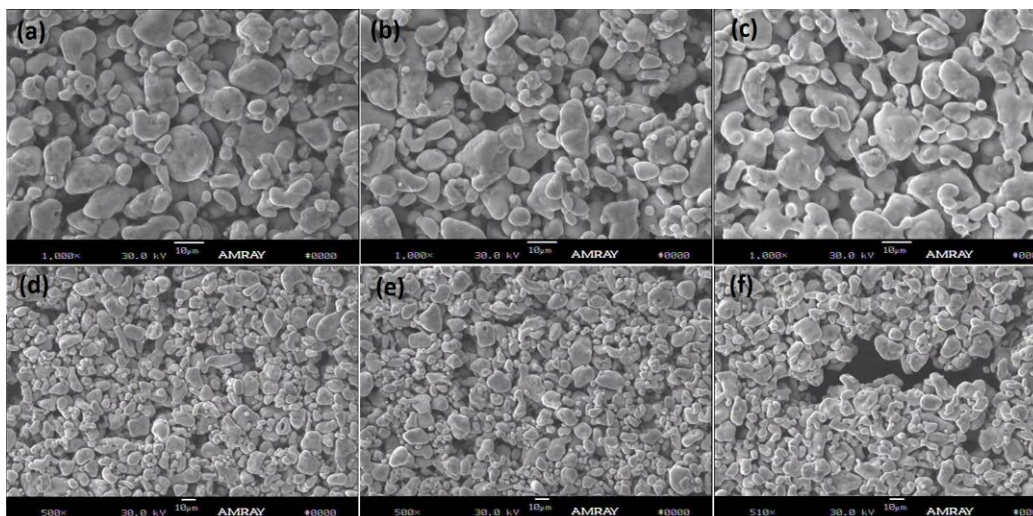


Fig. 27 SEM at 1000X Magnification Showing the Morphology of Sample test chips using 2:1 Cu: Ink Mass Ratio (a) SP_43 (b) SP_94 (c) SP_213 (Equipment AMRAY 1830)

3.8.2.2 Comparison of Pool Boiling Performance between Plain ship and Copper Porous Surfaces Created using Screen Printing Technique

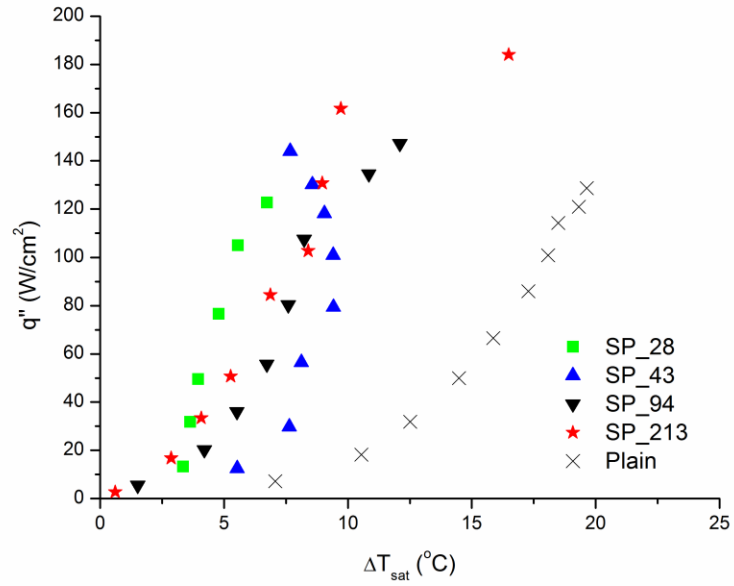


Fig. 28 Pool Boiling Curves for Plain and Copper Porous Surfaces Created using Screen Printing Technique

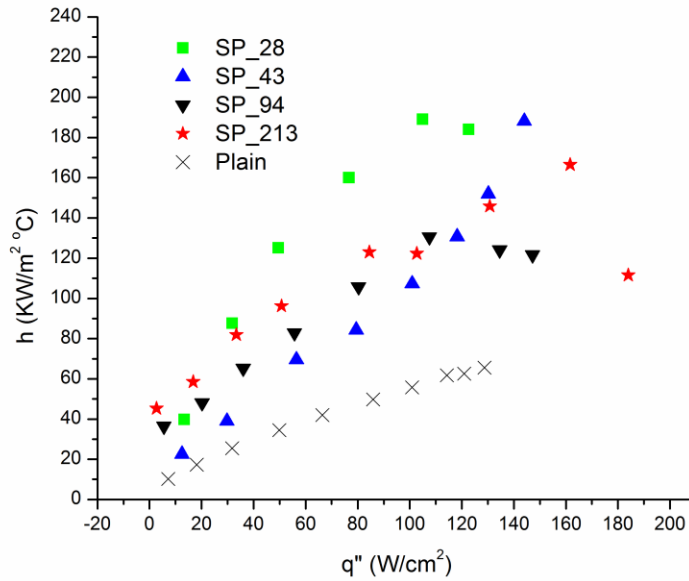


Fig. 29 Heat Transfer Coefficient Comparison for Plain and Copper Porous Surfaces Created using Screen Printing Technique

Comparison of pool boiling performance can be seen in Fig. 28 and Fig. 29. Pool boiling experiment was first done with plain test chip using distilled water at atmospheric pressure. This serves as a baseline for all enhancement comparisons. The highest CHF obtained in this group was 184 W/cm² (SP_213, 213 μm Coating thickness). The enhancement was approximately 43% in CHF over a plain test chip which had a CHF of 129 W/cm². The highest h obtained was 189 kW/m²°C which corresponds to an enhancement of 186% comparing to a plain test chip. Two observations can be made in this group. Firstly, as thickness increased, CHF increased as well. This trend will be discussed in detail in the following section. Furthermore, all copper porous surfaces enhancement pool boiling performance in CHF and h. This can be seen as a shift in pool boiling curves to the left. The results are consistent to the ones obtained using drop coating technique.

3.8.2.3 Effect of Coating Thickness on CHF Enhancement

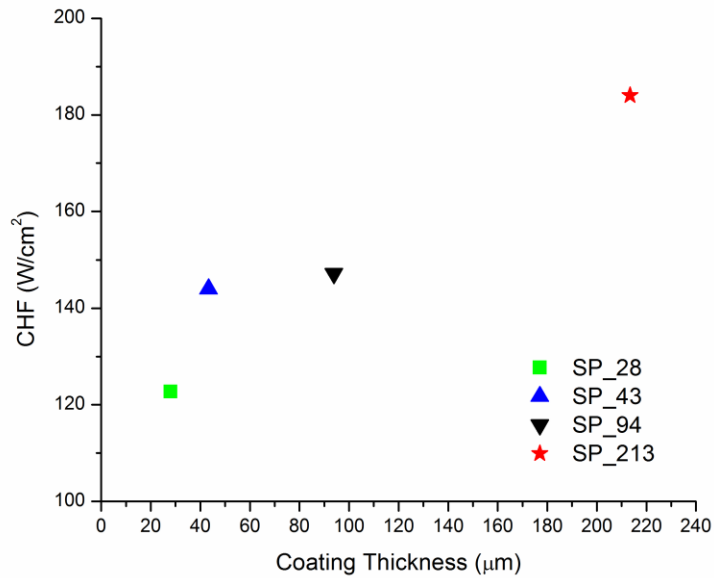


Fig. 30 Effect of Coating Thickness on CHF Enhancement

Fig. 30 shows a comparison of CHF obtained for different coating thickness. Overall, it can be seen that CHF increases with increasing coating thickness. The highest CHF obtained was 184 W/cm² for a coating thickness of 213 µm. The trend is consistent with the one observed in the drop coating study. Thin coatings with one or two layers of 3M copper powder does not enhancement CHF dramatically, but the h enhancement is evident due to its low thermal resistance. Researchers [15,27] propose that wickability of a porous surface play an important role on CHF enhancement. The ability to transport liquid through heated porous surface are expected to delay onset of CHF. Rahman et al.[27] quantified wickability of structured super-hydrophilic surfaces as the rate of decrease in liquid level as the pendant water droplet attached to a capillary tube contacted the test surface. Wicked volume flux was calculated to obtain an experimental correlation between wickability and

CHF. To understand the role of wickability of copper porous coating on CHF, a similar approach was adopted using the Sessile Drop Method.

3.8.2.4 Wickability Measurement

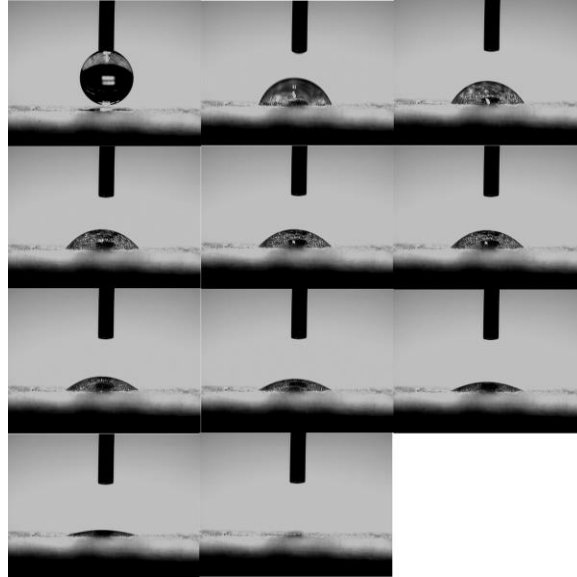


Fig. 31 Measurement of Wickability using Sessile Drop Method

Fig. 31 shows the measurement of wickability using Sessile Drop Method. A pendant water droplet was brought contact to the copper test surface. Due to its superhydrophilic characteristics, the contact angle would immediately decrease to zero. Using high speed recording, the rate of change in droplet volume can be measured on a frame by frame basis. This measurement was done for a selection of test surfaces (SP_28, SP_43, SP_94, SP_213) for the coating thickness study prior the pool boiling tests. A comparison can be seen in Table 9. Please note that the test chip is label with additional parameter wicking

rate. For example, SP_28_0.002 means the test surface has coating thickness 28 μm and wicking rate of 0.002 $\mu\text{l/s}$.

Table 9 Comparison of Wickability and CHF

Chip Label	Thickness (μm)	Wicking Rate ($\mu\text{l/s}$)	S.D. ($\mu\text{l/s}$)	CHF (W/cm^2)
SP_28_0.002	28	0.002	0.0002	122.7
SP_43_0.035	43	0.035	0.003	144.0
SP_94_0.106	94	0.106	0.047	147.2
SP_213_2.765	213	2.765	0.482	184.0

3.8.2.5 The Role of Wickability on CHF Enhancement

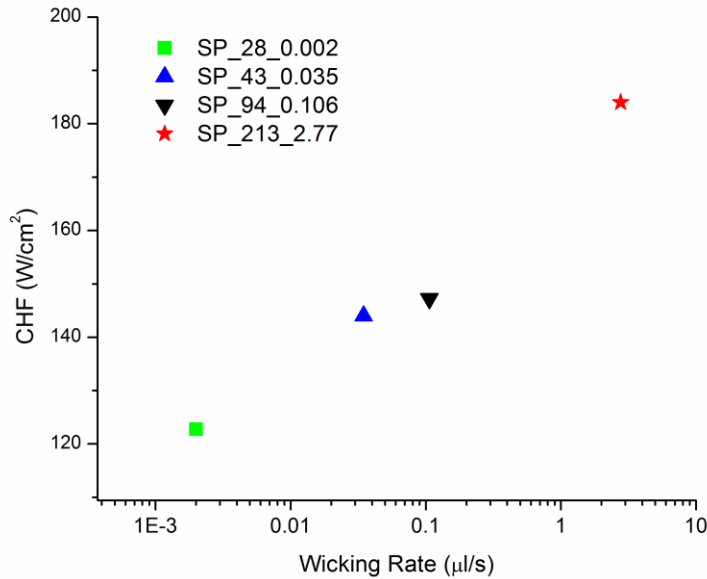


Fig. 32 Effect of Wickability and CHF Enhancement

Fig. 32 shows the CHF results for a selection of test chips in the previous study and the wickability measurement obtained. It shall be noted that the wickability was plotted on a logarithmic scale due to its large variation. As coating thickness increases, wickability was observed to increase as well. The highest wickability in rate of decrease of contact angle obtained was $2.765 \mu\text{l}/\text{s}$ for a $213 \mu\text{m}$ coating thickness. This corresponds to the highest CHF obtained in the coating thickness study. Hence, the enhancement in CHF due to increasing coating thickness can be attributed to its increasing wickability.

3.8.3 Visualization Research

High speed images provided further insight into the pool boiling enhancement of copper porous surface that's studied in the previous session. In this session, the comparison in pool boiling performance between SP_28 and SP_213 is discussed. Furthermore, the data extracted from high speed images were used to validate existing models to predict CHF.

3.8.3.1 SP_28 Pool Boiling Performance Analysis

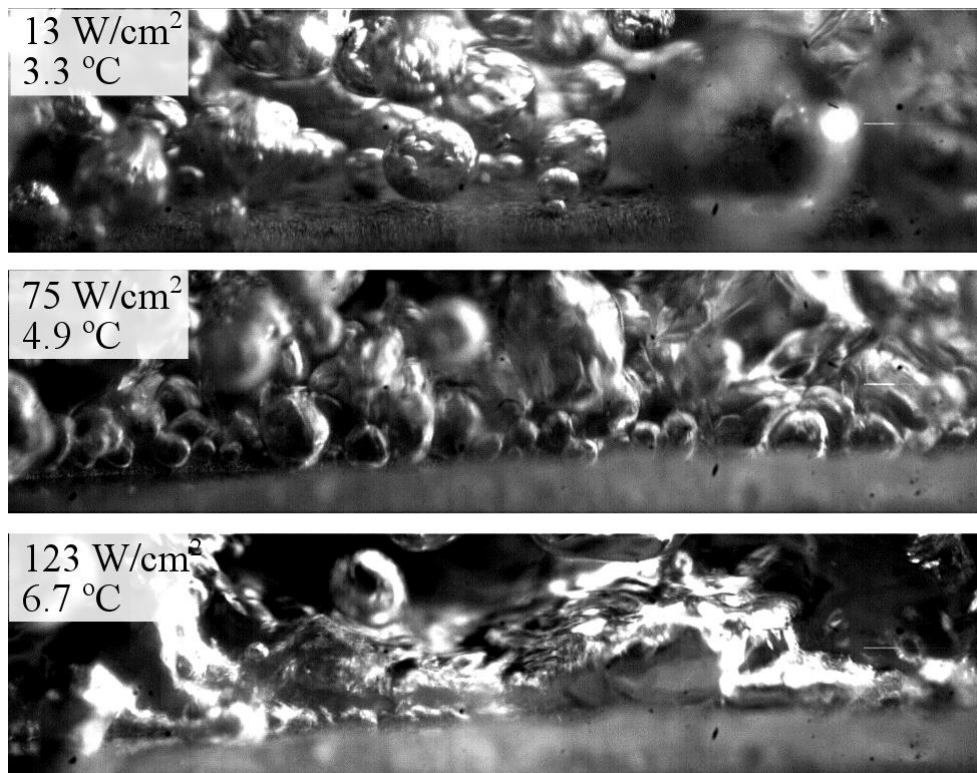


Fig. 33 SP_28 Pool Boiling High Speed Images at Different Heat Fluxes 8000fps

Fig. 33 shows high speed images of pool boiling for SP_28 at various heat fluxes. At a heat flux of 13W/cm², multiple nucleation sites can be seen on the copper porous surface. As wall super heat increases with increasing power input of the heater, more nucleation sites were activated. At heat flux of 75 W/cm², additional nucleation sites were observed on the

copper porous surface. This resulted in much lower wall superheat due to added agitation of the bubbles. This is consistent with the observation on the pool boiling curve as shown in Fig. 28 and Fig. 29 that at heat flux of 75 W/cm^2 , SP_28 has the highest h and lowest wall superheat. This suggests that nucleation site density plays a dominant role in enhancing pool boiling performance for thin copper porous surface. On the other hand, high nucleation site density can be a double edge sword at high heat flux region. As power input to the heater increases, bubble frequency and nucleation site density continue to increase. Nucleate boiling transition from partial boiling of discrete bubbles to fully developed region in which bubbles start coalescing laterally with other bubbles to form mushroom shaped bubbles. The coalescing behavior accelerated heater dry out. Soon a limit in heat removal is reached (CHF), as the heater is covered by a vapor blanket. The lateral coalescing behavior can be seen in the high speed image for heat flux at 123 W/cm^2 . Multiple stems of bubbles can be seen on the heater surface and all coalesced to form a much bigger bubble. Vigorous boiling behavior along with high vapor generation can be also observed on the image, suggesting that the CHF condition is imminent. The study in the role of wickability on CHF shows that at high heat flux condition, higher wicking rate helps delay heater dry out due to adequate liquid supply through the porous surface. Therefore, the low CHF limit obtained by SP_28 can be explained due to its poor wickability as compared to the thicker coating.

Furthermore, Hsu [22] developed a criteria on range of cavity radii at which nucleation can occur for a given wall superheat. Kandlikar [22] modified this equation by incorporating the effects of dynamic receding contact angle as shown below:

$$\{r_{cmin}, r_{cmax}\} = \frac{\delta_t \sin \theta_r}{2.2} \left(\frac{\Delta T_{sat}}{\Delta T_{sat} + \Delta T_{sub}} \right) \left[1 \mp \sqrt{1 - \frac{8.8 \sigma T_{sat} (\Delta T_{sat} + \Delta T_{sub})}{\rho_g h_{fg} \delta_t \Delta T_{sat}^2}} \right] \quad (7)$$

Table 10 shows the parameters and constants involved in this calculation.

Table 10 Parameters and Constants used for Water at Saturated Condition at Atmospheric Pressure Equation (7)

Parameter [Unit]	Name	Value
h_{fg} [kJ/kg]	Latent Heat of Vaporization - Water	2257
ρ_g [kg/m ³]	Density of Water Vapor at Saturated Condition	0.598
ρ_l [kg/m ³]	Density of Water Liquid at Saturated Condition	958.3
σ [N/m]	Surface Tension Water	0.0589
Tsat [°C]	Saturation Temperature Water	100
k_L [W/mK]	Thermal Conductivity of water	0.591
h [W/m ² K]	Single Phase Heat Transfer Coefficient water	5000
δ_t [m]	Liquid sublayer thickness assuming a linear temperature profile	0.000116

$\delta_t = \frac{k_L}{h}$, where k_L is the thermal conductivity of the liquid and h is the single-phase heat transfer coefficient in the liquid prior to nucleation.

The dynamic receding contact angle θ_r at multiple nucleation sites were measured for SP_28 as shown in Fig. 34. An average was taken to be to approximated 42°.

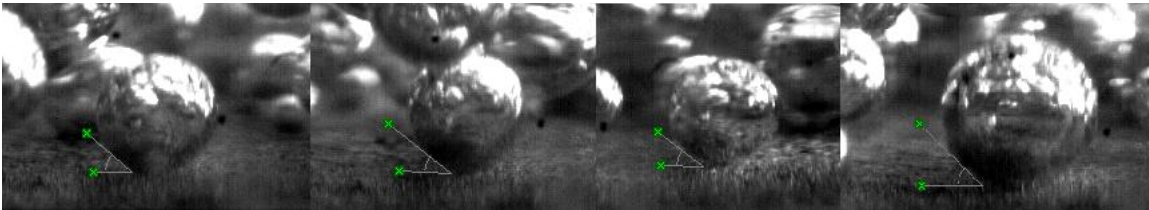


Fig. 34 Dynamic Receding Contact Angle Measurement SP_28

Hence the range of active cavity radii (r_{\min} , and r_{\max}) based on wall superheat for test chip SP_28 can be calculated.

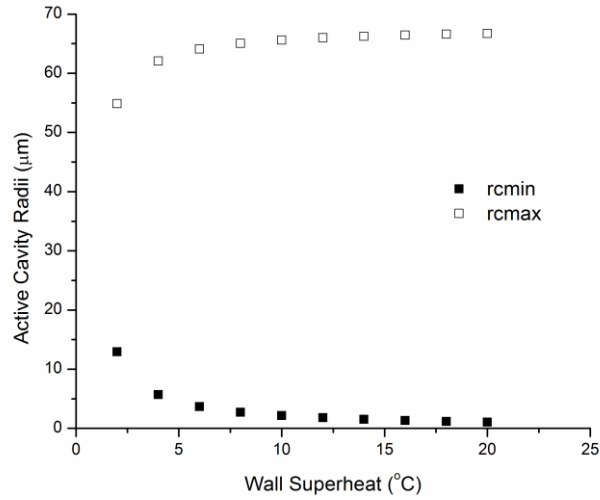


Fig. 35 Range of Active Cavity Radii for a wall superheat SP_28

Fig. 35 shows that as wall super heat increases from 4°C to 10°C, the minimum cavity radius needed for active nucleation lowered from 5.7 μm to 2.2 μm. SEM image of SP_28 in Fig. 36 showed that there are multiple pores openings that's below 5 μm in diameter. This suggests that at the wall superheat range, these open pores may be activated for boiling, resulting in enhancement in h.

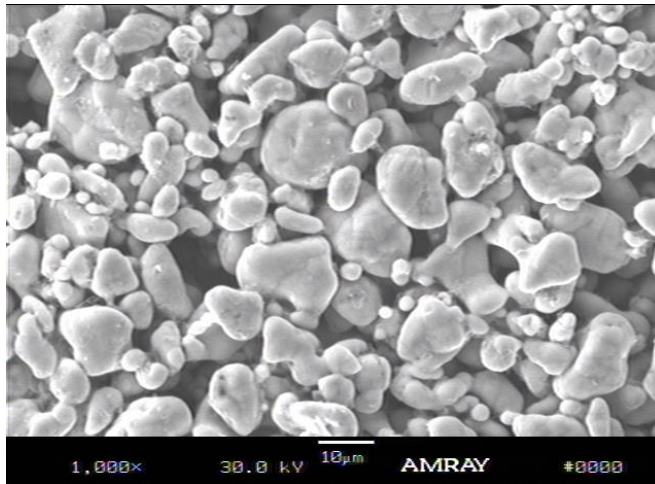


Fig. 36 SEM Image for SP_28 Showing Different Sizes of Cavity Radius

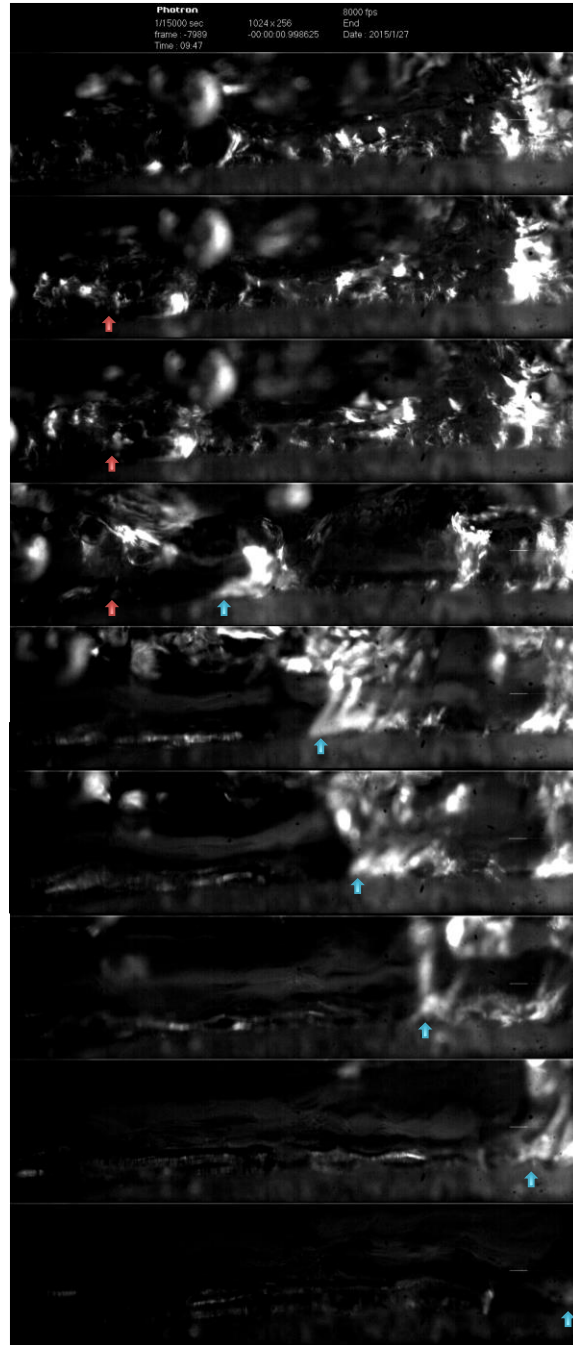


Fig. 37 CHF Visualization for Thin Coating (SP_28)

Fig. 37 shows a sequence of frame shots during CHF for test chip SP_28. This test ship has coating thickness of 28 μm and wickability of 0.09 Deg/s. The red arrow indicated the

location of a nucleation site and lateral growth was observed. The blue arrow indicated the movement of the vapor liquid interface. The observation is consistent with the CHF model developed by Kandlikar [29]. At CHF condition, the Evaporation Momentum Force overcomes the combined surface tension and hydrostatic forces along the heater surface. This results in lateral growth of vapor liquid interface along the heater surface and dry out is accelerated.

Furthermore Kandlikar's [29] model show that the CHF can be predicted based on the dynamic receding contact angle and the orientation of the heater surface.

$$q''_c = h_{fg} \rho_g^{\frac{1}{2}} \left(\frac{1 + \cos \theta_r}{16} \right) \left[\frac{2}{\pi} + \frac{\pi}{4} (1 + \cos \theta_r) \cos \phi \right]^{1/2} \times [\sigma g (\rho_l - \rho_g)]^{1/4} \quad (8)$$

Table 11 shows the parameters and constants involved with this equation (8)

Table 11 Parameters and Constants involved with Kandlikar's Model [22]

Parameter [Unit]	Name	Value
h_{fg} [kJ/kg]	Latent Heat of Vaporization - Water	2257
ρ_g [kg/m ³]	Density of Water vapor at Saturated Condition	0.598
ρ_l [kg/m ³]	Density of Water liquid at Saturated Condition	958.3
σ [N/m]	Surface Tension Water	0.0589
g [m/s ²]	Acceleration due to gravity	9.81
θ_r [Deg]	Measured Dynamic Receding Contact Angle	41.9
$q''_{CHF,CAL}$ [W/cm ²]	Calculated CHF based on Kandlikar's Model	131
$q''_{CHF,EXP}$ [W/cm ²]	Experimental CHF for SP_28	123

For horizontal heater surface $\phi = 0$.

The dynamic receding contact angle θ_r at multiple nucleation sites were measured for SP_28 as shown in Fig. 34. An average value was taken to be approximately 42° .

Hence, the CHF q''_c was calculated to be 130.7 W/cm^2 which was about 6% deviated from the measured value. The close prediction confirmed that surface wettability which is quantified by contact angle plays a dominant role in CHF condition for thin copper porous surfaces.

3.8.3.2 SP_213 Pool Boiling Performance Analysis

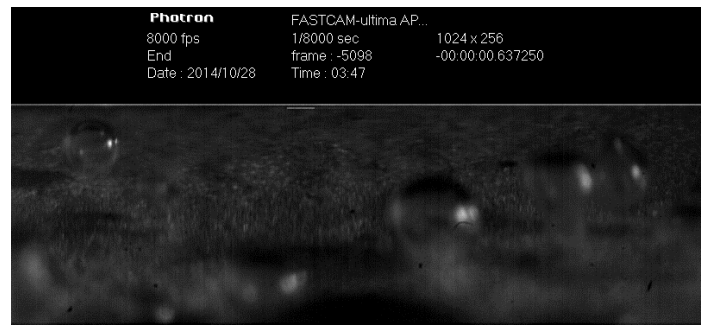


Fig. 38 High Speed Image showing Pool Boiling of SP_213 at Onset of Nucleation Boiling 8000 fps

Pool boiling curve of SP_213 ($213 \mu\text{m}$) in Fig. 28 shows that the test surface had a much earlier onset of nucleation boiling (ONB). This is confirmed by high speed images at 8000 fps. At wall superheat of 0.75°C , bubble nucleation was seen at multiple sites (Fig. 38). Heat flux at that moment was calculated to be 4.75 W/cm^2 .

Furthermore, Fig. 39 shows the high speed images of SP_213 during pool boiling at high heat fluxes. The red arrow points to the area of interest. At heat flux of 65 W/cm^2 and 125 W/cm^2 , partial nucleation boiling was observed in the location where discrete nucleation bubbles can be seen. The additional nucleation site activated at this moment help enhancing h as shown in Fig 28. Similar with SP_28, the pool boiling curve has a steep slope. At heat

flux of 180 W/cm^2 which is very close to CHF, fully developed nucleation boiling was observed. Firstly, the shape nucleating bubbles at the location were no longer recognizable due to increased bubble frequency at high heat flux. Furthermore, multiple bubbles were seen to coalesce with each other laterally to form bigger bubble. This resulted in a mushroom type bubble with several stems which is consistent with the description proposed by researchers [22] at this pool boiling region.

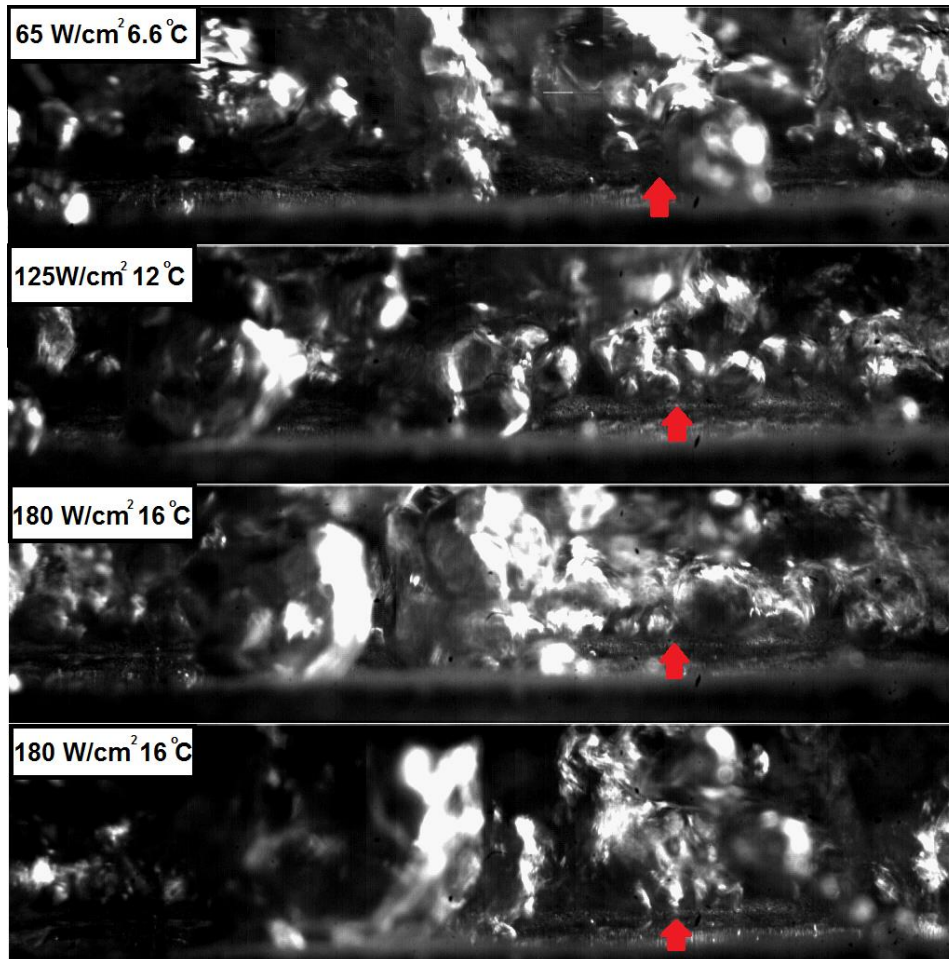


Figure 39 High Speed Images Showing Pool Boiling of SP_213 at High Heat Fluxes 8000 fps

The pool boiling behavior of SP_213 at CHF was also observed using high speed images at 8000fps (Fig. 40). It can be noted that some porous surface areas were still inactive in

spite of increased nucleation density at high heat flux close to CHF. These areas can be identified by the blue arrow on Fig.40. This suggested the area were constantly in contact with the liquid and transported the liquid through the porous surface due to capillary wicking. This observation is consistent with the idea of separated liquid and vapor pathway in the porous surface, proposed by Li et al. [15]. As vapor layer starts to form in the bottom of a thick porous surface, there can still be steadily nucleation boiling with liquid supply from the nearby wetted area. As seen in Fig. 28, Unlike SP_28, heat flux continued to increase with wall superheat at this region and dry out is significantly delayed.

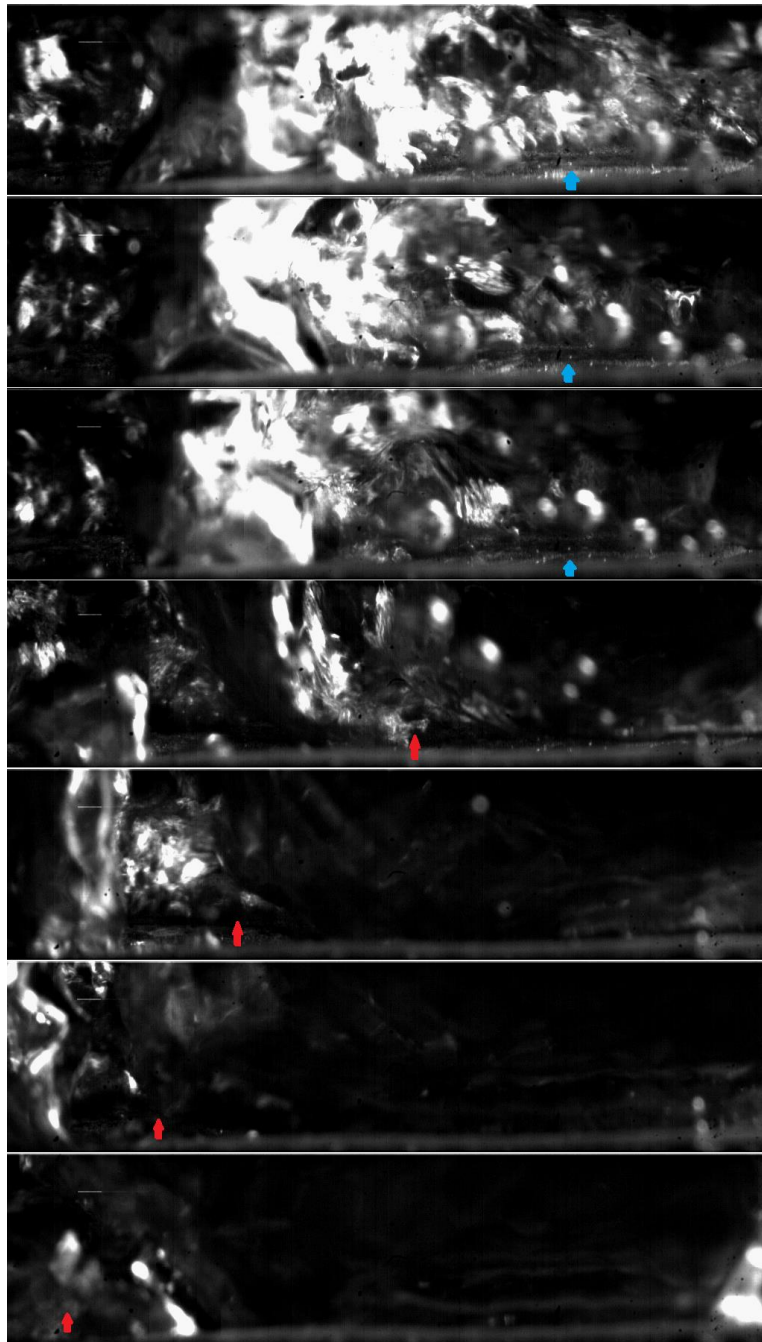


Figure 40 High Speed Images Showing SP_213 at CHF Condition 8000fps

Dynamic receding contact angle at a nucleation bubble was also measured using high speed images. As seen in Fig. 41, average measurement was taken to be approximately 30°.

Kandlikar's [22] model yielded a CHF of 143.6 W/cm² which is approximately 21% lower than the experimental value. This is consistent with literature that liquid supply due to capillary wicking contributes an additional portion of heat flux at CHF [27,30] for super hydrophilic surfaces.



Figure 41 Dynamic Receding Contact Angle Measurement for SP_213

Rahman et al. [27] proposed a CHF model with an enhancement factor that's based on the wickability of a super hydrophilic structured surface. As mentioned in the role of wickability study, the parameter was quantified by wicked volume flux through the wetted area when water pendant droplet was brought to contact the structured surface. They proposed a non-dimensional wicked volume flux as follows:

$$Wi = \frac{\dot{V}_0'' \rho_l}{\rho_v^{1/2} [\sigma g (\rho_l - \rho_v)]^{1/4}} \quad (8)$$

Where \dot{V}_0'' is the initial maximum volume flow rate and is calculated as follows:

$$\dot{V}_0'' = \frac{1}{A_w} \left(\frac{dV}{dt} \right)_{t=0} \quad (9)$$

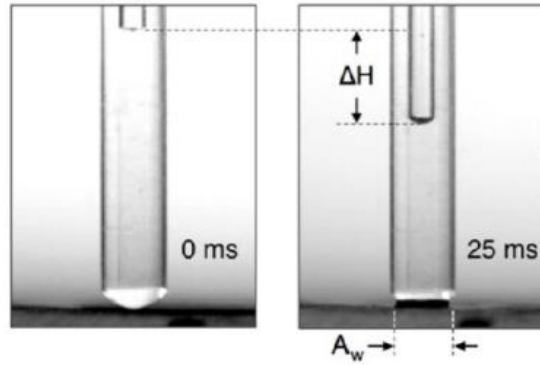


Figure 42 Wickability Measurement Done by Rahman et al.[27]

Fig.42 shows that A_w is the apparent wetted area and $\frac{dV}{dt}$ can be calculated based on ΔH

Furthermore, the predicted CHF $q_{CHF,W}''$ including the effect of wicking is proposed to be

$$\frac{q_{CHF,W}''}{q_{CHF,Zuber}''} = 1 + Wi \quad (10)$$

Where $q_{CHF,Zuber}''$ is a baseline CHF which is calculated to be 111 W/cm^2

Using Equation (8) (9) (10) , CHF $q_{CHF,W}''$ can be calculated for SP_213 using rate of decrease in contact angle as wicking rate. As shown in Fig.43, the wetted area A_w was



Figure 43 Wicking Rate Calculated by Rate of Decrease in Contact Angle

taken as the area where the water pendent droplet immediately contacted the porous surface. The volume of the liquid can be approximated based on the contact angle and the height of the water droplet on the porous surface. The change of volume of the liquid can

be approximated frame by frame using high speed camera. Therefore, the Initial Volumetric flux \dot{V}_0'' can be approximated based on the first two frames and was calculated to be approximated 5.16 mm/s. This corresponded to a Wi of 1.317 and a predicted $q_{CHF,W}''$ of 257 W/cm². Detailed parameters used for this calculation can be seen in Table 12. The model over predicted CHF obtained for SP_213 by approximated 40 %. However, the predicted CHF matched well with the structured surfaces selected by Rahman et al [27] as shown in . This goes to suggest that the model needs need further investigation to incorporate new type of structured surfaces such as copper porous surfaces.

Table 12 Parameters used to Calculated Predict CHF due to Capillary Wicking

Parameter [Unit]	Name	Value for Water
h_{fg} [kJ/kg]	Latent Heat of Vaporization	2257
ρ_g [kg/m ³]	Density of vapor at Saturated Condition	0.598
ρ_l [kg/m ³]	Density of Liquid at Saturated Condition	958.3
σ [N/m]	Surface Tension	0.0589
g [m/s ²]	Acceleration due to gravity	9.81
\dot{V}_0'' [mm/s]	Initial Volumetric Flux	5.16
A_w [mm ²]	Wetted Area on porous surface	0.772
Wi	Non-dimensional Wicked Volume Flux	1.318
$q_{CHF,W}''$ [W/cm ²]	Enhanced CHF due to capillary wicking	257
$q_{CHF,exp}''$ [W/cm ²]	Experimental Value CHF SP_213	184

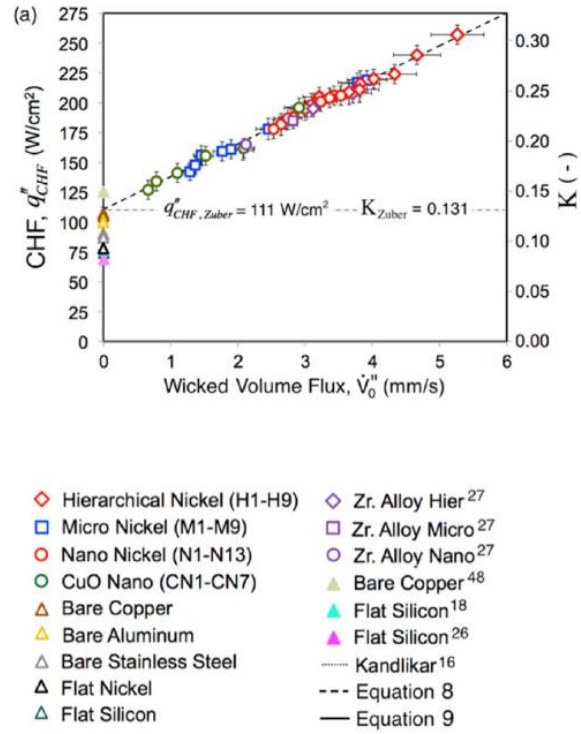


Figure 44 Experimental CHF as a function of Wicked Volume Flux [27]

Chapter 4 Conclusion

In this thesis, a two-part study was conducted to study the pool boiling enhancement of sintered copper porous surfaces. First, drop coating technique was used to deposit 3M L-20227 copper powder using a lost carbonate sintering process. The effect of coating thickness was investigated. The following key points are the summary for Part I of this study:

- (1) Sintered copper porous surface was successfully fabricated using a drop coating technique and a lost carbonate sintering process.
- (2) SEM images showed large open pores formed during sintering due to the presence of Na_2CO_3 .
- (3) Pool boiling test using distilled water at atmospheric pressure was conducted for 4 test surfaces. The highest CHF was obtained on test sample DC_447 (447 μm) to be 303 W/cm^2 at wall superheat of $33.8 \text{ }^\circ\text{C}$. This corresponds to approximately 135 % enhancement over the CHF obtained by a plain surface
- (4) As coating thickness increases, CHF was observed to increase as well.
- (5) All test sample in this study enhanced pool boiling in both CHF and h.

The coatings using drop coating technique were found to have poor coating thickness uniformity. To gain better control of thickness, a screen printing technique along with a working sintering recipe was developed. The following key point are the summary for part II of the study

- (1) Sintered copper porous surface was successfully fabricated using screen printing technique with commercial ink and a working sintering recipe was developed.

- (2) LCM and SEM images showed that the Cu:Ink mass ratio affect the morphology of the porous surface. A working ratio to produce sufficient coating uniformity was determined.
- (3) The effect of coating thickness on pool boiling performance was investigated again to validate the result found in earlier. The results were found to be consistent.
- (4) The study went further to investigate the role of wickability on CHF by measuring the rate of decrease in droplet volume as water pendant droplet make contact with the copper porous surface. CHF was found to be increasing with increasing wickability. This suggested that wickability played an important role in CHF enhancement.

High speed images for two surfaces tested in part II provided further insight into the pool boiling enhancement of sintered copper porous surfaces.

- (1) For a thin coating of 28 μm , high nucleation density is identified as the main contributing factor in enhancing h at high heat fluxes. However, inadequate liquid supply due to low wickability limited it the CHF enhancement. Furthermore, at CHF condition, lateral growth of vapor - liquid interface was observed. This is consistent with existing model which predicted CHF value based on dynamic receding contact angle.
- (5) For a thickness coating of 213 μm , earlier ONB was observed at low wall superheat. At low heat fluxes, the test sample performed similarly with the thin coating. At high heat fluxes, wetted area was observed near nucleation site. This suggested that adequate liquid supply was provided to the nucleation site due to high wickability

of the surface. As seen in the pool boiling curve, heat flux continued to increase with wall superheat. CHF is further delayed. Existing CHF models were used to compare predicted CHF with experimental value. Both Kandlikar's [29] and Rahman et al's [27] model yielded CHF with a large discrepancy. This calls for further investigation.

4.1. Recommendations for Future Work

- (1) A further investigation is needed to correctly predict CHF for sintered copper porous surface with high wickability
- (2) With current study as a baseline, an extensive parametric study can be done to optimize the pool boiling performance
- (3) The cross-linked open microchannel surfaces were seen to yield high CHF values. A combination of sintered copper porous surface and the cross-linked microchannel surfaces could enhance pool boiling even further.

Bibliography

- [1] Gurrum, S. P., Suman, S. K., Joshi, Y. K., and Fedorov, A. G., 2004, "Thermal issues in next-generation integrated circuits," *IEEE Trans. Device Mater. Reliab.*, **4**(4), pp. 709–714.
- [2] "Advances In High-Performance Cooling For Electronics «Electronics Cooling Magazine – Focused on Thermal Management, TIMs, Fans, Heat Sinks, CFD Software, LEDs/Lighting.»
- [3] Frank P, I., Theodore L, B., Adrienne S, L., and David P, D., 2011, "Fundamentals of Heat and Mass Transfer," *Fundamentals of Heat and Mass Transfer*, John Wiley & Sons.
- [4] Poniewski, M. E., and Thome, J. R., 2008, "Nucleate Boiling on Micro-Structured Surfaces."
- [5] Patil, C. M., and Kandlikar, S. G., 2014, "Review of the Manufacturing Techniques for Porous Surfaces Used in Enhanced Pool Boiling," *Heat Transf. Eng.*, **35**(10), pp. 887–902.
- [6] Li, C., and Peterson, G. P., 2007, "Parametric Study of Pool Boiling on Horizontal Highly Conductive Microporous Coated Surfaces," *J. Heat Transf.*, **129**(11), pp. 1465–1475.
- [7] Pivovar, R. E., 2009, "High Temperature Microporous Coatings: The Effects of Wetting and Wicking on Nucleate Boiling and CHF," The University of Texas at Arlington.
- [8] Kim, J. H., Rainey, K. N., You, S. M., and Pak, J. Y., 2002, "Mechanism of Nucleate Boiling Heat Transfer Enhancement From Microporous Surfaces in Saturated FC-72," *J. Heat Transf.*, **124**(3), pp. 500–506.
- [9] Fang, Z. Z., "Sintering of Advanced Materials - Fundamentals and Processes."
- [10] Zhao, Y. Y., Fung, T., Zhang, L. P., and Zhang, F. L., 2005, "Lost carbonate sintering process for manufacturing metal foams," *Scr. Mater.*, **52**(4), pp. 295–298.
- [11] Hanlon, M. A., and Ma, H. B., 2003, "Evaporation Heat Transfer in Sintered Porous Media," *J. Heat Transf.*, **125**(4), pp. 644–652.
- [12] Ahmed, Y. M. Z., Riad, M. I., Sayed, A. S., Ahlam, M. K., and Shalabi, M. E. H., 2007, "Correlation between factors controlling preparation of porous copper via sintering technique using experimental design," *Powder Technol.*, **175**(1), pp. 48–54.
- [13] Li, X.-B., Tang, Y., Li, Y., Zhou, S.-Z., and Zeng, Z., 2010, "Sintering technology for micro heat pipe with sintered wick," *J. Cent. South Univ. Technol.*, **17**(1), pp. 102–109.
- [14] Mao-Yu Wen, Ching-Yen Ho, and Kang-Jang Jang, 2012, "Characteristics of pool boiling heat transfer from sintered surfaces," *Adv. Mater. Res.*, **566**, pp. 382–5.
- [15] Li, C., Peterson, G. P., and Wang, Y., 2006, "Evaporation/Boiling in Thin Capillary Wicks (I)—Wick Thickness Effects," *J. Heat Transf.*, **128**(12), pp. 1312–1319.
- [16] Tuma, P., "L-20227 Application."

- [17] Chang, J. Y., and You, S. M., 1997, "Enhanced boiling heat transfer from microporous surfaces: effects of a coating composition and method," *Int. J. Heat Mass Transf.*, **40**(18), pp. 4449–4460.
- [18] Yao, Z., Lu, Y.-W., and Kandlikar, S. G., 2011, "Direct growth of copper nanowires on a substrate for boiling applications," *IET Micro Nano Lett.*, **6**(7), pp. 563–566.
- [19] Li, C., and Peterson, G. P., 2010, "Geometric Effects on Critical Heat Flux on Horizontal Microporous Coatings," *J. Thermophys. Heat Transf.*, **24**(3), pp. 449–455.
- [20] Yao, Z., Lu, Y.-W., and Kandlikar, S. G., 2013, "Pool Boiling Heat Transfer Enhancement Through Nanostructures on Silicon Microchannels," *J. Nanotechnol. Eng. Med.*, **3**(3), pp. 031002–031002.
- [21] McHale, J. P., Garimella, S. V., Fisher, T. S., and Powell, G. A., 2011, "Pool boiling performance comparison of smooth and sintered copper surfaces with and without carbon nanotubes," *Nanoscale Microscale Thermophys. Eng.*, **15**(3), pp. 133–150.
- [22] Kandlikar, S. G., Dhir, V. K., and Shoji, M., 1999, *Handbook of Phase Change : Boiling and Condensation*, Taylor and Francis, Ann Arbor, MI.
- [23] Bergles, A. E., and Chyu, M. C., 1982, "Characteristics of Nucleate Pool Boiling From Porous Metallic Coatings," *J. Heat Transf.*, **104**(2), pp. 279–285.
- [24] O'Hanley, H., Coyle, C., Buongiorno, J., McKrell, T., Hu, L.-W., Rubner, M., and Cohen, R., 2013, "Separate effects of surface roughness, wettability, and porosity on the boiling critical heat flux," *Appl. Phys. Lett.*, **103**(2), p. 24102.
- [25] Ahn, H. S., Park, G., Kim, J. M., Kim, J., and Kim, M. H., 2012, "The effect of water absorption on critical heat flux enhancement during pool boiling," *Exp. Therm. Fluid Sci.*, **42**, pp. 187–195.
- [26] Bon, B., Klausner, J. F., and McKenna, E., 2013, "The Hoodoo: A New Surface Structure for Enhanced Boiling Heat Transfer," *J. Therm. Sci. Eng. Appl.*, **5**(1), pp. 011003–011003.
- [27] Rahman, M. M., Ölçeroğlu, E., and McCarthy, M., 2014, "Role of Wickability on the Critical Heat Flux of Structured Superhydrophilic Surfaces," *Langmuir*, **30**(37), pp. 11225–11234.
- [28] Xu, P., Li, Q., and Xuan, Y., 2015, "Enhanced boiling heat transfer on composite porous surface," *Int. J. Heat Mass Transf.*, **80**, pp. 107–114.
- [29] Kandlikar, S. G., 2001, "A Theoretical Model to Predict Pool Boiling CHF Incorporating Effects of Contact Angle and Orientation," *J. Heat Transf.*, **123**(6), pp. 1071–1079.
- [30] Ahn, H. S., Lee, C., Kim, J., and Kim, M. H., 2012, "The effect of capillary wicking action of micro/nano structures on pool boiling critical heat flux," *Int. J. Heat Mass Transf.*, **55**(1–3), pp. 89–92.